Lawrence Berkeley National Laboratory
Lawrence Berkeley National Laboratory

Title

MICROSTRUCTURES AND PHASE TRANSFORMATIONS IN INTERSTITIAL ALLOYS OF TANTALUM

Permalink

https://escholarship.org/uc/item/3d84d0d5

Author

Dahmen, U.

Publication Date

1979

Peer reviewed

MICROSTRUCTURES AND PHASE TRANSFORMATIONS IN INTERSTITIAL ALLOYS OF TANTALUM

Ulrich Dahmen
(Ph. D. thesis)

January 1979

MASTER

MICROSTRUCTURES AND PHASE TRANSFORMATIONS

IN INTERSTITIAL ALLOYS OF TANTALUM

by

Ulrich Dahmen

Lawrence Berkeley Laboratory
University of California
Berkeley, California 94720

TABLE OF CONTENTS

MICROSTRUCTURES AND PHASE TRANSFORMATIONS

IN INTERSTITIAL ALLOYS OF TANTALUM

by

Ulrich Dahmen

ABSTRACT

The analysis of microstructures, phases, and possible ordering of interstitial solute atoms is fundamental to an understanding of the properties of metal-interstitial alloys in general. As evidenced by the controversies on phase transformations in the particular system tantalum-carbon, our understanding of this class of alloys is inferior to our knowledge of substitutional metal alloys. The present study is an experimental clarification of these controversies in tantalum. Using advanced techniques of electron microscopy and ultrahigh vacuum technology, an understanding of the microstructures and phase transformations in dilute interstitial tantalum-carbon alloys is developed.

Through a number of control experiments, the role and sources of interstitial contamination in the alloy preparation (and under operating conditions) are revealed. It is demonstrated that all previously published work on the dilute interstitially ordered phase $Ta_{64}C$ can be explained consistently in terms of ordering of the interstitial contaminants oxygen and hydrogen, leading to the formation of the phases $Ta_{12}O$ and Ta_2H .

In contrast to previous work on Ta–C , and in agreement with studies on Nb–C and V–C , no dilute ordered phases are observed. Instead, the precipitation of carbon from supersaturated solution in tantalum, is found to be a multistage process involving the homogeneous nucleation of metastable coherent precipitates on {310} matrix planes and their growth to the final incoherent carbide Ta_2C . A careful analysis of the experimental evidence yields the significant result that interstitial carbon co-precipitates with tantalum lattice vacancies. An application of this result to other refractory metal–carbon systems is capable of accounting for previously unexplained results on the age-hardening behavior of these alloys. Postulating a vacancy trapping mechanism, a hypothesis is developed, which is consistent with all the experimental work on refractory metal–interstitial system surveyed. A number of experiments are suggested designed to test this hypothesis.

The coherent carbide is shown to lose coherency during growth by dislocation loop punching. The morphology, internal defect structure and interface structure of the incoherent ordered carbide β–Ta_2C is investigated experimentally. An accurate determination of the orientation relationship between the bcc matrix (m) and the hexagonal precipitates (p) yields $(1\bar{1}01)_p \| (10\bar{1})_m$ and $[11\bar{2}0]_p \| [25,\bar{26},25]_m$. Applying a minimum energy model to the growth of these incoherent precipitates, their rod like morphology is explained. The same model is shown to be successful in predicting the radically different morphologies in a number of similar precipitation systems investigated before.

Professor G. Thomas
Department of Materials Science and
Mineral Engineering

1. Introduction

In spite of their technological importance, metal–interstitial systems have received relatively little attention in metallurgical research. Probably all metals contain small amounts of interstitial solids such as hydrogen, oxygen, nitrogen and carbon because they are present in abundance in the environment. Of the many technologies that involve interstitial solutes in metals, those of steel and nuclear materials are only two prominent examples. The hardening of steel, hydrogen embrittlement, structural stability in a radiation environment and many other processes are directly related to metal–interstitial interactions. Yet the effects of such interstitial elements on the properties of their host metals are far less understood than those of substitutional elements. With the exception of steel, where interstitial carbon is utilized extensively, these effects are usually taken into account only by empirical overall correction factors. In titanium, for example, the oxygen equivalent is a factor which relates the strengthening and embrittlement resulting from additions of oxygen to those of other interstitials. Such empirical factors ignore the individual microstructures and mechanisms of interaction that lead to the changes in properties.

A systematic study of metal–interstitial systems that would provide a microstructural and thermodynamic understanding of stable and metastable phases is needed. This understanding would ultimately make it possible to utilize interstitial elements in the design of alloys with desired properties rather than treat these interstitials as unavoidable impurities.

The present work is a small step towards such an understanding. It is a systematic study of the precipitation behavior of carbon in

dilute tantalum-carbon alloys. The microstructures and phase transfor-
mations in these alloys have been studied by different groups[1-6] result-
ing in some unexplained differences. Specifically, the problem of the
ordered $Ta_{64}C$ phase, first reported by Villagrana and Thomas[1,2], was
a point of controversy. It was the most dilute of all known ordered
phases and was confirmed by Rao and Thomas[4,5], who related the onset
of the precipitation of this phase to a drastic embrittlement of the
alloy. A later study by Seetharaman et al.[6] also confirmed the crystal
structure but differed on the morphology. Such controversies are not
uncommon in metal-interstitial systems, as demonstrated for example by
the literature on the vanadium-oxygen[7-10] or the tantalum-oxygen
system[11-17]. In the particular case of $Ta_{64}C$, the solution was
strikingly simple and surprising. However the process of finding the
correct result was by no means straightforward. It led over an inves-
tigation of phase transformations in tantalum-hydrogen and tantalum-
oxygen alloys to the final tantalum-carbon system.

In this thesis, for the sake of clarity, the results are presented
in order of their significance rather than chronologically. Although
the behavior of tantalum-carbon alloys was established and explained
only in the last part of the thesis research, it sets the stage for an
understanding of earlier studies. The results on tantalum-carbon will
therefore be presented first and with the most detail. This part also
contains the most important findings of this research. Hence the dis-
cussion is almost entirely centered on these results.

The results on tantalum-hydrogen and tantalum-oxygen alloys will
be treated more briefly in the second and third part of the experimental
results. These two sections essentially grew out of control experiments

and literature research done before the work on the actual tantalum-carbon system. Both hydrides and oxides may form as a result of contamination of pure or carbon-doped tantalum during the sample preparation. Since they are produced by distinctly different sources of contamination and because their microstructures are characteristically different, the hydride and the oxide are treated in two separate sections. These two sections hold the clue to the solution of the existing controversy on the tantalum-carbon alloys. Only those results which are new and pertinent to this controversy are reported. A brief description of the experimental procedures used and a short discussion of the most interesting results is included, so that these two sections are actually self-contained. Thus they may be read either separately or in the context of the results on the carbide precipitation. Even though the discussion section is primarily concerned with the tantalum-carbon system, the importance of contamination by hydrogen or oxygen should not be underestimated. As one of the refractory metals, tantalum is applied mainly as a structural material under high temperature / high vacuum conditions[18]. These are precisely the conditions investigated and discussed here. With the recent focus on the refractory metals as possible first wall reactor materials, an understanding of the micro-structural effects of contamination is even more important.

The discussion represents a synthesis of both the findings of this research and those of the literature concerning phase transformations in refractory metal-interstitial systems in general. The experimental evidence obtained for the coherent precipitates leads to the formulation of a hypothetical vacancy trapping mechanism while the evidence presented on incoherent precipitates is discussed in terms of a modified

existing model. Both models are shown to be of much wider applicability
than only the tantalum-carbon system, and a brief list of the mo᷈ᷛ import-
ant implications and future experiments is given.

2.   Experimental Procedure

The materials were prepared from 99.9 wt.-% pure tantalum by elec-
tron beam zone refining in a vacuum of about 10^{-6} torr. After three
passes, the single crystal rod of 8 mm diameter was rolled into a sheet
of 150 μm thickness. The sheet was cut into pieces 60 mm long and 25 mm
wide, followed by cleaning and chemical thinning to 100 μm in a mixture
of 25% HF and 75% HNO_3 and finally washing in methanol. The intersti-
tial impurity content at this stage as determined by chemical analysis
was 0.02 ± 0.03 at.-% hydrogen, 0.01 ± 0.01 at.-% oxygen, 0.05 ± 0.01 at.-%
nitrogen and 0.02 ± 0.02 at.-% carbon.

2.1 Alloying with carbon

In order to reproduce the experimental conditions previously
reported in the literature for Ta-C alloys, and since no experimental
apparatus was available that would allow carburization from the gas
phase, the somewhat tedious method of vapor deposition of carbon onto
pure tantalum followed by a vacuum diffusion anneal was adopted. The
mass and thickness of the carbon layer to be deposited were estimated
as follows.

$$W_C = \frac{c_C}{100} \times W_{Ta} \times \frac{w_C}{w_{Ta}}$$

where W_i is the total weight of component i in the sample, w_i the
atomic weight of component i and c_C the ca   n concentration in
at.-%. For a typical weight of the tantalum sample of 1500 mg, and with
$\frac{w_C}{w_{Ta}} = \frac{1}{15}$, a mass W_C of 1 mg should be deposited for a concentration

of one at.-% carbon. Since the reproducibility of different weighings on a precision balance was found to be only 0.3 mg (corresponding to 0.3 at.-% carbon), the thickness of the deposited film was taken as an alternative measure of the final carbon concentration. The desired film thickness was estimated as

$$t_C = t_{Ta} \times \frac{v_C}{v_{Ta}} \times \frac{c_C}{100}$$

where t_C and t_{Ta} are the thicknesses of the carbon film and the tantalum sheet, respectively, and v_i are the atomic volumes, (v_C is taken here as 5.68 $Å^3$, the atomic volume of carbon in diamond, leading to a lower limit expression for t_C). With a thickness of the tantalum sheet of $t_{Ta} = 100$ µm , a value of $t_C \gtrsim 3150$ Å per at.-% carbon is obtained. The film thickness was measured with an estimated accuracy of ±100 Å in an optical interference microscope using a control sample coated with a reflective layer of aluminum. These error limits correspond to a more accurate ±0.03 at.-% carbon.

The carbon was deposited in up to 20 layers, each layer about 350 Å thick, with a distance of 85 mm between source and samples. This distance was found experimentally as a compromise between overheating of the samples with subsequent decohesion of the film at shorter distances and decreasing coverage at larger distances. (The film thickness decreases with increasing source distance r as $\frac{dt}{dr} \alpha \frac{1}{r^3}$.) The pressure before evaporation was 5×10^{-5} torr. After each layer, the vacuum had to be broken in order to replace the carbon electrode. Equal amounts of carbon were deposited on both sides of the metal sheet.

Such diffusion couples were then annealed in a vacuum of 10^{-6} torr for homogenization. The temperatures were chosen so as to reproduce earlier work reported in the literature[5,6], i.e., 2 hours at 2000°C followed by 24 hours at 800°C, and 72 hours at 1400°C. After the heat treatment, the material was furnace cooled at a rate of about 1°C per second.

Chemical analysis of the homogenized material showed that the carbon content of a sample coated with ~3000 Å of carbon was 0.5 ± 0.02 at.-% carbon instead of the estimated 0.95 at.-%. This shows that appreciable decarburization takes place during vacuum annealing at 10^{-6} torr. The microstructures produced by the above heat treatments were of poor reproducibility and inconsistent with the results of previous work produced under identical conditions. Since the group Va metals are very sensitive to contamination, even at low pressures, the experiments were continued in ultrahigh vacuum $(p \leqslant 10^{-8}$ torr) in order to obtain better reproducibility.

2.2 Ultrahigh vacuum (UHV) heat treatments

The reason for using a UHV system for the heat treatments is twofold; in addition to reduced contamination, a highly efficient refinement can be achieved. Gaseous impurities like hydrogen, nitrogen and oxygen which dissolve exothermally in tantalum, are removed from the metal at high temperatures and low pressures by outgassing. This is shown below, using the thermodynamic data from the literature[19]. The reaction

$$\frac{1}{2} I_2 \text{ (gas)} \rightleftharpoons I \text{ (solution)} \tag{1}$$
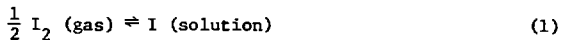
has a standard free energy change of

$$\Delta G_I^O = \Delta H_I^O - T\Delta S_I^O \; ,$$

where ΔH_I^O and ΔS_I^O are the heat and entropy of solution. At equilibrium,

$$\Delta G_I^O = - RT \ln K \; .$$

(R gas constant, T absolute temperature, and K equilibrium constant). For the reaction (1), K is given by

$$K = \frac{a_I}{\sqrt{p_{I_2}}}$$

where a_I is the activity of element I in interstitial solution at a concentration c_I , and p_{I_2} is the pressure of the diatomic gas I_2 in dynamic equilibrium with the solution. In the ideal solution range of low concentrations,

$$a_I = 10^{-2} \, c_I$$

where c_I is the atomic concentration of I in Ta . The equilibrium constant is then

$$K = \frac{10^{-2} c_I}{\sqrt{p_{I_2}}}$$

which is the well-known Sievert's law. It states that the concentration c_I is proportional to the square root of the gas pressure p_{I_2}. The proportionality constant is a function of temperature. The expression for c_I can now be written as

$$c_I = 100 \sqrt{p_{I_2}} \exp\left(\frac{\Delta S_I^O}{R}\right) \exp\left(-\frac{\Delta H^O}{RT}\right) .$$

Since ΔH^O is negative (exothermic solution), c_I decreases with increasing temperature; c_I also decreases with decreasing pressure (Sievert's law). A heat treatment in high vacuum at high temperature can therefore reduce the concentrations of these gaseous solutes to insignificant levels as shown in the following.

For hydrogen, $\quad \Delta S_H^O = -14.0$ cal/mole

$$\Delta H_H^O = -8690 \text{ cal/mole} \times \text{deg.}$$

At 500°C and 10^{-8} torr

$$c_H = 7.9 \times 10^{-5} \text{ at.-\%} .$$

For nitrogen, $\quad \Delta S_N^O = -14.4$ cal/mole

$$\Delta H_N^O = -43500 \text{ cal/mole} \times \text{deg.}$$

At 2100°C and 10^{-8} torr

$$c_N = 2.5 \quad 10^{-3} \text{ at.-\% .}$$

For oxygen, $\Delta S_O^O = -22.9 \text{ cal/mole}$

$$\Delta H_O^O = -91500 \text{ cal/mole deg.}$$

at 1800°C and 10^{-8} torr

$$C_O = 15.8 \text{ at.-\% ,}$$

which is beyond the solubility limit of 5.6 at.-% at this temperature.
However, above 1700°C, tantalum forms the volatile oxides TaO and
TaO_2 . The oxide molecules condense on the cold walls of the vacuum
system, and no equilibrium oxide gas pressure is built up. A steady
state between the oxygen loss by this irreversible reaction

$$Ta(s) + O \text{ (solution)} \rightarrow TaO(g)$$
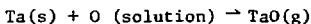
and the reversible reaction

$$\frac{1}{2} O_2(g) \rightleftharpoons O \text{ (solution)}$$
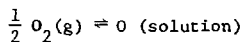
is established. This leads to a steady state concentration

$$c_O = 2.03 \times 10^{-3} \; p_{O_2} \; \exp\left(\frac{68350}{RT}\right) .$$

At $2100°C$ and 10^{-8} torr

$$c_0 = 4.0 \times 10^{-5} \text{ at.-}\% \quad \text{(extrapolated from } p = 5 \times 10^{-5} \text{ torr)}$$

These considerations show that in an ultrahigh vacuum of 10^{-8} torr and a homogenizing temperature of $2100°C$, the concentrations of the gaseous impurities hydrogen, nitrogen and oxygen in tantalum are reduced below 2.5×10^{-3} at.-%. This is less than 0.5% of the lowest carbon content. It should be emphasized that little or no outgassing is expected for carbon in UHV, because it is a solid and does not form any volatile carbides with tantalum, and the oxygen pressure is too low to lead to an appreciable loss of carbon by the formation of CO. The solubility limit of carbon at $2100°C$ is 2.21 at.-%[20], well above the carbon concentrations of 0.5–1.0 at.-% used in this research.

The apparatus used was the one described in ref. 20. A series of pumps evacuates the stainless steel specimen chamber. The specimen is clamped across two feedthrough copper electrodes. A high ac current passed directly through the specimen causes Joule heating.

Temperatures up to the melting point of tantalum (~3000°C) could be reached by this method. The temperature profile along the specimen was parabolic. In order to avoid melting of the copper contacts, the samples were cut in the shape of a tensile specimen. The gauge length was 10 mm, the width 3 mm, and 5 mm at the ends. The total length was 30 mm and the thickness 100 μm, as before.

Pressures below 10^{-8} torr were obtained after baking the system for 12 hours at 200°C. The specimen temperature was measured through a viewing port with an optical pyrometer. The spectral emissivity data

of ref. 21 were used to correct the measured gray body temperature.
Below 800°C, a 75 μm W–5% Re/W–26% Re thermocouple, spotwelded to the
tantalum sample, was employed to measure the temperature. By comparison
of the two methods, the accuracy of the pyrometric measurements was
found to be about ±20°C.

All samples were homogenized and outgassed for 1 hour at 2100°C.
They were then quenched by switching off the heating current. According
to the results of Westmacott and Peck[20], the quenching rate was about
2500°C sec^{-1}. Subsequent annealing was done at various temperatures
without braking the vacuum.

2.3 Thermotransport

A thermodynamic factor that had to be considered, was the possi-
bility of setting up a concentration gradient due to the temperature
gradient inherent in the direct heating method[22]. With the specimen
geometry described above, the temperature gradient near the center was
always less than 40°C mm^{-1}, as measured pyrometrically. The possible
influence on the carbon concentration was estimated to be negligible,
as shown below.

At steady state, the flux of carbon due to the temperature gradient
is compensated by the flux down the resulting concentration gradient

$$\frac{D_C c_C Q_C^*}{RT^2} \frac{dT}{dx} = - D_C \frac{dc_C}{dx}$$

or

$$\frac{d(\ln c_C)}{dx} = \frac{Q_C^*}{R} \frac{d\left(\frac{1}{T}\right)}{dx}$$

where

Q_C^*:   heat of transport for carbon in Ta

c_C: carbon concentration

R: gas constant

T: temperature

x: distance from the point of maximum temperature (center)

A simple solution is obtained for a linear temperature profile[22)]

$$\frac{dT}{dx} = \frac{(T_o - T_\ell)}{\ell}$$

(1)
$$c_C(x) = \frac{c_o B}{1 - \exp(-B)} \exp\left(-B \frac{x}{\ell}\right)$$

where

$$B = \frac{Q_C^*}{R} \frac{(T_o - T_\ell)}{\ell}$$

T_o: temperature at   x = 0

T_ℓ: temperature at   x = ℓ

Equation (1) shows that the concentration of carbon would be a minimum at the point of highest temperature if Q_C^* were negative and vice versa. Unfortunately, no values for Q_C^* are available. By comparison with Q_C^* in other materials[19)], the limits

$$- 4.5 \ \frac{kcal}{mole} < Q_C^* \ (\text{in Ta}) < + 4.5 \ \frac{kcal}{mole}$$

are reasonable. With the above assumption of a linear temperature gradient and $\Delta T = 200°C$, the carbon concentration would vary by less than 5% of the mean concentration ($c_o \pm 0.05 \ c_o$) in the specimen range of interest. Thermomigration should therefore be insignificant in the experimental setup used.

2.4 Specimen thinning for electron microscopy

After the heat treatments, one 3 mm disc was punched from each of the 5 mm regions on both sides of the sample center. They were jet polished in a solution of 4 vol.-% H_2SO_4 in methanol at $-30 \pm 5°C$. The current density was 1A cm^{-2}. The distance between the jets was 30 mm. With the electrolyte just covering the jets, the flow speed was adjusted to a steady laminar flow just causing a surface ripple in the center between the two jets. Using this technique, uniform electron transparent areas were obtained around the center of the foil with good reproducibility. Another polishing technique, used unitially and in previous research, was chemical thinning in a solution of 25 vol.-% HF in HNO_3. This technique was abandoned because of its preferential attack of the carbide precipitates and the hydrogen contamination caused by the chemicals (see results).

2.5 Electron microscopy

The electron microscopy was done with a Siemens 102 microscope (125 kV) with high angle tilt and high resolution capabilities and a Philips 301 (100 kV) with a single tilt cooling stage. Discussions of

the techniques employed are given in the literature; see ref. 23 for conventional diffraction contrast, refs. 24,25 for loop analysis, ref. 26 for the weak beam technique and refs. 27,28 for the high resolution lattice imaging technique.

3.   Experimental Results

3.1   The supersaturated solution

As described in the preceding section, a very high quenching rate
of $2500°C \ sec^{-1}$ could be obtained by switching off the heating current
after homogenizing in ultrahigh v··:uum.   All carbon was held in super-
saturated solution as evidenced by fig. 1 which shows an example of such
a quenched foil. Only a few isolated dislocations are present.
Apparently, no heterogeneous nucleation has occurred at the dislocations.
Note the strongly mottled background. This mottling is not observed ⁴.
fully aged foils polished under identical conditons, i.e., it is char-
acteristic of the supersaturated solution. A similar background struc-
ture was observed in as quenched solutions of carbon in vanadium[29,30] and
carbon in niobium[31,32]. If this structure is due to small carbon clus-
ters, they are at this stage too small or not localized enough to be
resolved individually. Even in a high resolution two beam lattice image
of one set of {110} planes, no small scale defects can be detected in
such a foil (see fig. 2b). It is unlikely that more information could
be obtained with any other set of {110} planes diffracting since dif-
fraction patterns from as quenched foils are completely symmetrical
(fig. 2a) with no observable streaking or directionality.

3.2   The coherent carbide

Ageing the as-quenched material in ultrahigh vacuum at about 400°C
for 144 hours, produces a microstructure as shown in fig. 3. A large
number of small platelike precipitates have formed. They are about
300 Å in size. The plane of the plates, as determined by careful trace
analysis, is the {310} matrix plane. There are twelve equivalent {310}

planes resulting in an almost random appearance of the plate habit. These precipitates are very similar to the ones found in the Nb-C and the V-C systems after a similar quench-ageing sequence[29-32]. As in these two systems, the precipitates here are coherent. From fig. 3 and a number of other micrographs, their density was determined to be on the order of 10^{15} cm^{-3}.

Evidently, the particles have precipitated homogeneously, since they are distributed evenly and are not attached to any visible lattice defects. In fact, depleted zones occur around lattice defects such as grain boundaries and dislocations. In fig. 3, for example, a precipitate free zone of about 500 Å width can be seen around the dislocation.

Due to the small volume fraction of the precipitate phase and due to the low scattering power of carbon, no extra spots are expected in the diffraction patterns. This was confirmed by all the diffraction patterns of the material in this state. The (001) section in fig. 4a is a typical example of these patterns. For this reason, the structure of the precipitates, if different from bcc , cannot be determined directly at this time.

Although the (001) pattern in fig. 4a contains four ⟨310⟩ directions, perpendicular to four sets of precipitate plates, no streaks were detected even at the longest exposure times. Yet the platelets appear to be very thin in the micrographs, similar to planar GP zones (as for example in Al-Cu alloys[33]). This absence of streaking can be explained if it is assumed that small deviations from the exact {310} habit and/or the perfect precipitate structure occur. The shape transform of such imperfect plates would give a spread in intensity sufficient to make streaks undetectable far away from the Bragg reflections.

In the immediate vicinity of the Bragg reflections, the ⟨310⟩ streaks should be more localized. However, they are too weak to be distinguished from the diffuse background (see fig. 4a). Their presence can be shown by tilting the foil a few degrees away from a symmetrical low index orientation like (001) in fig. 4a. This is shown in fig. 4b where the foil has been tilted by 15.8° around the [110] axis to the (1$\bar{1}$5) orientation. The (1$\bar{1}$0) intensity (encircled) is seen in a weak, well defined spot. Since the (1$\bar{1}$0) reflection is at a distance of 0.13 Å^{-1} from the Ewald sphere, it can only been seen if its elongation (streaking) is at least this distance. This corresponds to the shape transform of a diffracting crystal of a maximum thicknes of 8 Å[23] (about 8 {310} planes). From the same micrograph, the lower limit to the crystal shape can be found to be about 4 Å (~4 {310} planes) from the absence of intensity at the (2$\bar{2}$0) position.

A dark field image of the encircled streak (perpendicular to the plane of the pattern) shows that the intensity indeed arises from the precipitates, fig. 5. C ly those precipitates appear bright which are nearly perpendicular to the beam direction. This micrograph, and the fact that the observed crystal is flat is evidence for the estimate given above.

Since the precipitates are very small, their main contrast features in electron microscopy are indirect, resulting from their effect on the matrix lattice. From this point of view, the particles may be treated as matrix defects, i.e., dislocation loops Such additional information can be gained from this procedure. The following micrographs show how the nature and magnitude of the displacement field near a precipitate can be determined by standard techniques of electron microscopy. This

information can then be used in turn to deduce the structure and mecha-
nísm of formation of the precipitates.

3.3 Loop analysis of the coherent carbide

If the displacement vector (Burgers vector) of a dislocation loop
is equal to a lattice translation (perfect loop), no contrast will be
seen inside the loop. If the Burgers vector is only a fraction of a
lattice vector (faulted loop) the loop will show straight black and
white fringes. The best-known example of this type of fringe contrast
are stacking fault fringes. In general, the depth periodicity of the
contrast is equal to the extinction distance of the operating (matrix)
reflection. On a BF micrograph as in fig. 6b, no fringe contrast is
seen inside the loops. However, it cannot be concluded that the preci-
pitates may be described as perfect loops because their size is smaller
than one extinction distance ($\xi_{110}^{Ta} \simeq 500$ Å)[23] and no fringes are
expected even for _faulted_ loops of this size. Making use of the weak
beam technique[26] the effective extinction distance can be reduced as
shown in fig. 6a. The same loops as in fig. 6b now show fringes which
are parallel to the imaginary intersection of the loop plane with the
surface. Thus the different {310} habit planes can be distinguished by
their fringe directions. From fig. 6a, it can be concluded that the
displacement vector is not a perfect lattice vector. In the loop
analogy, the precipitates correspond to faulted loops.

Applying the effect of inside/outside contrast which occurs for
dislocation loops when the operating g-vector is reversed, the sense of
the Burgers vector can be found[24]. If at the same time, the specific
indices of the loop plane are known by tilting the loop edge-on, it can
be determined whether it is interstitial or vacancy in character[25].

Figure 7 shows such a contrast experiment. The first four pictures (a,b,c,d) are near the (001) pole, the last two (e and f) near the (101) pole, after a 45° tilt. All six micrographs are taken in the bright field mode under two-beam conditions with a positive deviation s from the Bragg condition. Loops on three different {310} planes are marked A, B and C . In an (001) orientation, four sets of {310} planes are parallel to the electron beam, namely (310), ($3\bar{1}0$), (130) and ($\bar{1}30$). From trace analysis, loops A are found to lie on (310) planes. Loops B and C are inclined with respect to the electron beam. Their habit planes can be determined by relating their change in projected width to the sense and magnitude of tilt. B is thus found to be on a (30⊥) and C on a (103) plane.

The direction and magnitude of the displacement vector and the character of the loops can now be deduced in turn. Take loop B which lies on a (301) plane. It is out of contrast in $\underset{\sim}{g} = (0\bar{2}0)$, shows strong contrast in $\underset{\sim}{g} = (\bar{2}00)$ and medium contrast in both $\underset{\sim}{g} = (\bar{1}\bar{1}0)$ and $\underset{\sim}{g} = (\bar{1}10)$ as well as in $\underset{\sim}{g} = (10\bar{1})$ and $\underset{\sim}{g} = (\bar{1}01)$. This is consistent with a displacement vector $\underset{\sim}{R}$ parallel to the loop normal, i.e., $\underset{\sim}{R} = \frac{1}{n} [301]$. The same argument shows that the displacement vector for loop C is consistent with $\underset{\sim}{R} = \frac{1}{n} [103]$. This can be seen more clearly in table 1 which lists the product $\underset{\sim}{g} \cdot \underset{\sim}{R}$ for the g vectors used in fig. 7 and for $\underset{\sim}{R}$ parallel to the loop plane normals of loops A,B,C .

R \ g	$[\bar{1}\bar{1}0]$	$[\bar{2}00]$	$[1\bar{1}0]$	$[0\bar{2}0]$	$[10\bar{1}]$	
$\pm\frac{1}{n}$ [310]	$\pm\frac{2}{n}$	$\pm\frac{6}{n}$	$\pm\frac{2}{n}$	$\pm\frac{2}{n}$	$\pm\frac{3}{n}$	
$\pm\frac{1}{n}$ [301]	$\pm\frac{3}{n}$	$\pm\frac{6}{n}$	$\pm\frac{3}{n}$	0	$\pm\frac{2}{n}$	Table 1
$\pm\frac{1}{n}$ [103]	$\pm\frac{1}{n}$	$\pm\frac{2}{n}$	$\pm\frac{1}{n}$	0	$\pm\frac{2}{r}$	

Thus the loops are shown to be pure edge loops, i.e., they are areas in which material has been added or removed with no or little shear involved.

In order to find the approximate magnitude of the displacement, again consider table 1. The observed contrast, proportional to $g \cdot R$, can be compared with the contrast of loops with known displacement vector in the same material. Here, the comparison was made with images of glide loops with $R = \frac{a}{2}\langle\bar{1}1\bar{1}\rangle$ (see loops marked * in fig. 8). $g \cdot R$ is equal to 1 in fig. 8a and 2 in fig. 8b. The contrast in the former is similar to loops A in figs. 7e and f. If $g \cdot R$ is set equal to 1 for these loops, R comes out to be $\frac{1}{3}$ [310] . Although this procedure lacks accuracy, it is reliable and quantitative enough to yield the significant result that the magnitude of the displacement vectors is near $\frac{1}{3}\langle310\rangle$. This is supported by the displacement fringe contrast shown earlier in fig. 6a, since $\frac{1}{3}\langle310\rangle$ is not a perfect lattice translation and leads to a faulted rather than a perfect loop.

A third and rather important piece of information about the precipitates that can be obtained by means of the loop analogy is the character of the loop, i.e. the sense of the displacement field. Föll and Wilkens[25] have devised a simple procedure which allows the determination of the loop character by a tilt series like fig. 7. Consider loops A

in figs. 7e and f. They appear smaller in fig. 7e than in 7f. Thus
they show inside contrast in $g = (10\bar{1})$. According to the Föll/Wilken-
rules, this means that $(g \cdot R)s > 0$, i.e., $\left([10\bar{1}] \cdot \frac{\pm 1}{3} [310]\right)s > 0$.
Since $s > 0$, the specific indices of the displacement vector for loop
A are $+\frac{1}{3}$ [310]. By tilting the foil in a known sense until loop A
is seen edge-on (figs. 7a,b,c,d), here from a (101) to an (001) orienta-
tion, the specific indices of the loop plane normal $\underset{\sim}{m}$ ($\underset{\sim}{m} = +$ or $- [310]$)
can be found. The positive sense of the loop plane normal $\underset{\sim}{m}$ is defined
here as that (+ or −) [310] direction which makes an acute angle with
the direction pointing towards the electron source. For loops A in
figs. 7e and f, this is +[310].

The second of the Föll/Wilkens rules states that loops are of
vacancy type if $\underset{\sim}{R} \cdot \underset{\sim}{m} > 0$. This is the case here where $\underset{\sim}{R} \cdot \underset{\sim}{m} =$
$\frac{1}{3}$ [310] · [310] > 0.

The same result is obtained for the other loops, B and C. C
for example shows outside contrast in $g = (10\bar{1})$, i.e. $\underset{\sim}{R} = +\frac{1}{3}$ [103].
By tilting, $\underset{\sim}{m}$ is found to be +[103], therefore $\underset{\sim}{R} \cdot \underset{\sim}{m} > \underset{\sim}{0}$, as before.
The precipitates can hence be described as faulted vacancy type disloca-
tion loops. The lattice is locally relaxed towards the precipitate
rather than being compressed as one would expect for the clustering of
interstitial atoms. This is a rather surprising result and no such
effect has been reported before in the literature on bcc metals,
although recently a similar type of precipitates was observed in
quenched fcc platinum[34]. The most reasonable explanation of this
phenomenon is the hypothesis that tantalum lattice vacancies and inter-
stitial carbon atoms precipitate together to produce an overall effect

of lattice relaxation, analogous to the co-precipitation of vacancies
and carbon in fcc platinum[34]. The significance of such a mechanism
will be discussed in detail later.

3.4 Growth of the coherent precipitates

Although clear from previous experience, it remains to be demon-
strated that the loops are actually precipitates. Rather than by theo-
retical contrast calculations, this was done by ageing the same alloy
for 17 hours at the higher temperature of about 500°C after a rapid
quench in ultrahigh vacuum. Figure 9 shows a grain boundary in such a
foil.   The precipitates have lost their loop contrast and have grown
to a slightly larger size. Note the precipitate-free zone on both sides
of the boundary. The width of this zone was found to be about 1 µm and
uniform along all grain boundaries examined. No precipitates were
detected in the grain boundaries or at triple junctions, even at the
highest magnifications. This observation lends strong support to the
hypothesis of a vacancy-carbon co-precipitation. A grain boundary is
a perfect sink for vacancies so that even at high rates of quenching,
a zone depleted of vacancies will form adjacent to the boundary.
Annealing a quenched sample such that only short range diffusion of car-
bon is possible will then result in the observed microstructure. Small
metastable coherent carbon precipitates can nucleate semi-homogeneously,
i.e., with the aid of lattice vacancies. In vacancy-depleted areas, no
nucleation is possible. At the same time, heterogeneous nucleation does
not take place because of the long-range diffusion required.

As is already apparent in fig. 9, ageing for 17 hours at ~500°C
leads to a homogeneous distribution of larger precipitates. This is
more readily visible in fig. 10 which shows a microstructure typical

for this stage of the transformation. The precipitates have grown to a size of about 500 Å. They exhibit large strain fields which are an indication of their coherency with the matrix. From this as well as a number of other micrographs, it seems apparent that the precipitates have lost their plate-like character, i.e., growth between this and the preceding stage is mostly a thickening of the platelets or a one-dimensional process. Most precipitates are associated with a lattice dislocation, a fact which could indicate the beginning of the loss of coherency, a mechanism that becomes much more pronounced in a later stage of ageing. The background shows a uniform mottled structure, less obvious than in the as-quenched state. This mottling only appears at the $s = 0$ diffracting condition and is not visible in the coherency strain fields. It remains to be investigated whether this is a bulk or a surface effect.

A more important question here is that of the precipitate structure. Some of the particles in fig. 10 show an irregular internal structure. The origin of this structure could be displacement fringes due to matrix deformation alone, Moiré fringes due to interfering diffraction from both matrix and precipitates, or due to internal faulting of the precipitates themselves. In the first case, there is no diffraction from the precipitates, in the last two cases, they diffract and give rise to extra spots in the diffraction pattern. The diffraction pattern in fig. 11 shows the latter to be true. Faint extra spots are observed at the marked positions. By careful measurement of their spacings, using the matrix spots as an internal standard, they can be identified as diffraction spots from the hexagonal Ta_2C phase. They are indexed according to the lattice parameter data given in ref. 35. It can be concluded that at this stage of the precipitation, the particles have

adopted the equilibrium Ta_2C structure, a fact that becomes more obvious as the particles grow.

Knowing that the precipitates give rise to observable diffraction intensitites, their internal structure can only be a result of faulting or Moiré interference. The two high magnification views of the structure of a particular precipitate in different diffracting conditions (fig. 11) show a distinct change of this structure, typical for Moiré fringes. This is consistent with the fact that no streaking of the Ta_2C spots is apparent in the diffraction pattern, as it would occur in the case of planar faulting. Hence fig. 11 shows that the observed fringe structure in the coherent particles is mainly, if not entirely, due to Moiré interference. This is in agreement with the precipitation of V_2C in V[29] but in contrast to Nb_2C in Nb[32].

No internal faulting was detected in two-beam high resolution lattice images, as in fig. 12. The area shown in this figure is marked by a circle in the inset lower magnification view of the entire precipitate. Such a fringe image of the {110} matrix planes is more interesting in terms of local variations in fringe spacing of the matrix fringes which might indicate local changes in carbon concentration. After ref. 36, the lattice parameter of tantalum changes by 0.04% per at.-% carbon. Assuming a total depletion near the precipitate and a maximum of 0.3 at.-% C at a distance from the precipitate, the lattice parameter should change from 3.303 to 3.307 Å, i.e. the {110} fringe spacing varies from 2.336Å to 2.338 Å. To measure such a small change in fringe spacing, much of the spatial resolution of a lattice image has to be sacrificed[78]. If an accuracy of ±0.2 d is assumed in measuring a single fringe spacing d , an average over a minimum number of 2000 fringes has to be

taken in order to obtain the required accuracy of ±0.01 %. Since the
average particle size is about 500 Å, and the average interparticle spac-
ing about 2000 Å, such a measurement would become meaningless. This
point is borne out by careful measurements on the actual micrographs,
for example, fig. 12. The measured fringe spacing varies only within
the error limits of the measurements.

3.5 Loss of coherency

Ageing the material for 144 hours at an even higher temperature of
800°C after a rapid quench produces a microstructure as shown in fig. 13.
Large needle or rod shaped precipitates of the equilibrium Ta_2C hexag-
onal structure are surrounded by dense dislocation tangles. These tangles
form networks with almost dislocation free areas in between. The appear-
ance and scale of these networks or cells is reminiscent of the well
known phenomenon of polygonization. Most of the particles are elongated
along $\langle 112 \rangle$ directions. Their sizes vary from 0.2 to 5 μm.

Although the microstructure in low magnification micrographs of
thick foils is more representative of the bulk, it is difficult to deter-
mine the actual shape and size of the precipitates because they are not
easily distinguished from the closely surrounding network of dislocations.
Figure 14 shows a precipitate in a thinner part of the same foil.
Apparently, most dislocations have slipped out of the foil. The shape
of the precipitate is now visible more clearly. In conjunction with
the correctly oriented and indexed diffraction pattern, the particle
can be seen to be short in the [0001] direction and elongated along a
direction in the (0001) plane. The wavy lines in the background are
Moiré fringes. They are mainly perpendicular to [110]/[0001] and their
spacing D is consistent with the one expected for interference of

(110) and (0002) beams: $D = \dfrac{d_{110}\ d_{0002}}{d_{0002} - d_{110}} \simeq 50$ Å . Some faint spots
(indexed (0001)) due to carbon ordering are also visible in the diffraction pattern. The observed carbide phase is thus the low temperature ordered β-Ta$_2$C phase (fig. 15)[37)] in which the carbon atoms occupy every other layer of interstitial sites between basal planes in the hexagonal metal lattice. Figure 15 also shows some other hexagonal carbide or nitride structures with different types of interstitial ordering but the same stoichiometry. L$_3'$ Random is the high temperature disordered α-Ta$_2$C structure.

These ordered β-Ta$_2$C precipitates were also foun.. in all slowly cooled alloys. The density of dislocations is lower than in the quench-aged material, and no cell formation is observed. Figure 16 shows the microstructure after slow cooling from 2000°C. The precipitate is about 3000 Å in length, and a string of dislocation loops obviously punched out by the particle is apparent. The same type of defect structure was reported to occur in the Nb-C and V-C systems[29-32)]. It was shown there that this was a result of the increase in atomic volume through precipitation, and not of the difference in ther...l expansion of the precipitate and matrix phases. The same mechanism is likely to be responsible in the present system, since the relative increase in volume ($\Delta V_V = +18\%$, $\Delta V_{Nb} = +17\%$, $\Delta V_{Ta} = +15\%$) is very similar in the three precipitation systems. The shape of the precipitate in fig. 16 is again rod or needle like.

The same configuration is found for the material when furnace cooled (about $1°C\ sec^{-1}$) from the lower temperature of 1400°C, as in ref. 6, see fig. 17. As in the previous cases, an elongated precipitate is surrounded by dislocations some of which are clearly loops intersecting

the surface, see curved arrow. An interesting phenomenon is manifested in the double string of loop-like features (straight arrow). A contrast experiment of these features is shown in fig. 18. The small "loops" are precipitates since they do not show straight, but irregular fringe contrast in a weak beam micrograph (fig. 18e). These precipitates are seen to be encircled by dislocation loops. From earlier results, it is clear that the precipitates are too small (~200 Å) to have lost coherency by dislocation punching. Hence they cannot be the origin of the dislocation loops surrounding them. It is therefore likely that these are secondary precipitates nucleated inside a set of glide loops punched out earlier in the cooling process by a larger, growing precipitate. Under the reasonable assumption that the loops have interstitial character (the atomic volume increases in the precipitation), the growth of these loops by climb will result in the production of vacancies which were shown earlier to aid the nucleation of metastable coherent precipitates. Although the suggested mechanism rests on several assumptions, it is a plausible one, considering the fact that such vacancy-aided precipitation in the wake of climbing dislocations has been reported before[38]. However, a definite proof of this type of secondary nucleation awaits further experimentation.

Since it was shown in the last three micrographs that the morphology of the incoherent Ta_2C precipitates and the dislocation substructure is qualitatively the same in the quench-aged and the slow cooled material, all the following results are taken from the more easily produced slowly cooled material.

While in the preceding results of this section, the deformation of the surrounding matrix has been documented as a way in which the transformation strains are accommodated, a more complete analysis has

to take into account other possibilities of accommodation, such as a fixed orientation relationship between matrix and precipitate structure, a particular particle shape, faulting and defects in the precipitate itself or in its interface with the matrix. These factors are treated in turn in the following paragraphs.

3.6 Orientation relationship

Even though the hexagonal equilibrium Ta_2C precipitates are incoherent with the matrix, they follow an orientation relationship close to the one found for the martensitic transformation of zirconium from bcc to hcp[39] . A number of composite matrix and precipitate diffraction patterns were taken in different orientations. Some of these are reproduced in figs. 20, 21, 22. Their analysis leads to the orientation relationship given in the composite stereographic projection of fig. 19. The stereographic projection of hexagonal β-Ta_2C with a c/a-ratio of 1.592 was plotted accurately with the aid of a computer program[40]. Great circles containing major poles are marked as dashed lines for the Ta_2C structure and as solid lines for the superimposed cubic structure of the tantalum matrix. Poles of the hexagonal structure are marked by open circles and indexed in the four-index Miller-Bravais notation; the cubic poles are marked by solid circles and the indices are written in italics. This orientation relationship can be written as

$$(\bar{1}101) \| (10\bar{1})$$

and

$$[11\bar{2}0] \| [26,\overline{25},26]$$

The close packed planes (0001) and (110) are within 1.5° of being paral-
lel, the close packed directions [11$\bar{2}$0] and [1$\bar{1}$1] are rotated by 1°.
Figures 20, 21 and 22 show how this is deduced from matrix-precipitate
composite diffraction patterns in different low-index orientations.

In order to relate these diffraction patterns directly to their
corresponding great circles in the stereographic projection, simplified
versions of fig. 19 are shown with each set of low index spot patterns
in figs. 20, 21 and 22. For example, the stereogram in fig. 20d shows
the great circles of the diffraction patterns in fig. 20a,b,c, with
great circles dashed for the hexagonal structure and solid for the cubic
structure. The orientation relationship can thus be verified directly
in each figure. It should be noted that even though the great circles
of the two structures do not coincide, the corresponding zones can be
observed simultaneously in the diffraction patterns even if their zone
axes make an angle of several degrees. This is a result of the relaxa-
tion of the Laue conditions due to the finite size of the diffracting
crystals. All diffraction patterns are indexed consistent with the spe-
cific orientation relationship in fig. 19.

It is now easy to see from figs. 20b and 22a that the close packed
basal plane (0001) in Ta$_2$C is not parallel to the close packed (110)
plane in Ta . In both diffraction patterns, a small rotation is appar-
ent between the (0002) and the (110) diffraction spots. The full rota-
tion of 1.5° is seen in the (1$\bar{1}$1) pattern while only a fraction of 1° or
less is seen in the (001) pattern. These angles are reproduced by the
angles between (0001) and (110) on the two great circles corresponding
to the (1$\bar{1}$1) and the (00$\bar{1}$) zones. The fact that almost no misorientation
is seen in a (1$\bar{1}$1) zone (fig. 20a) is also clear from the stereogram.

The angle between (0001) and $(\bar{1}101)$ in Ta_2C is 61.45° while (110) and $(10\bar{1})$ are rotated by 60°. Thus with (0001) at 1.5° from (110), the $(\bar{1}101)$ and the $(10\bar{1})$ poles should coincide exactly. That this is actually the case, is shown experimentally in figs. 20b, 20c and 21a. In none of these diffraction patterns is there any noticeable misorientation between those two spots. In fact, the spots virtually coincide because the spacing of the $(\bar{1}101)$ planes (2.36 Å) is very close to the $(10\bar{1})$ spacing (2.34 Å). Referring to the simplified stereograms or to fig. 19, it is seen that each of these three spot patterns views these two parallel planes from a different angle. This parallelism is also confirmed by the $(0\bar{1}0)$ pattern in fig. 25 (cf. stereographic projection in fig. 22b). It is thus shown uniquely that $(\bar{1}101)$ is exactly parallel to $(10\bar{1})$.

With this point firmly established, the relative orientation of directions within these planes can be determined in a $(10\bar{1})$ zone. This orientation is shown in fig. 21c. A 1° rotation between the $(\bar{1}103)$ and the (121) spots is apparent. This is equivalent to a 1° rotation of the $[\overline{11}20]$ direction from $[\bar{1}1\bar{1}]$ towards [010], which can also be measured on the same micrographs (see arrowed directions). The rotation between these two close packed directions completes the orientation relationship.

By careful analysis of a number of composite diffraction patterns, it is thus proved that the orientation relationship is the one shown in fig. 19 with

$$(\bar{1}101) \| (10\bar{1})$$

and

$$[11\bar{2}0] \| [26,\overline{25},26] \ .$$

Neither the close packed planes nor the close packed directions are
exactly parallel. The only set of planes which are exactly parallel in
this orientation relationship is $(\bar{1}101)$ $(10\bar{1})$, a pyramid plane in the
hexagonal structure with a close packed plane in the cubic structure.
A very similar orientation relationship has been reported for the preci-
pitation systems V_3N-V[41], Nb_2N-Nb[42] and Ta_2N-Ta[42], where the
same two planes are parallel and the rotation between the close packed
directions is about two degrees. However, the systems Nb_2C-Nb[32],
V_2C-V[29] and W_2C-W[43] which are very similar to the Ta_2C-Ta system,
exhibit a different orientation relationship, one in which close packed
planes and directions are exactly parallel, i.e., the Burgers relation-
ship with

$$(000\bar{1}) \| (110)$$

and

$$[11\bar{2}0] \| [1\bar{1}1]$$

While the reported orientation relationship is one means of minimiz-
ing the transformation stresses, other means were observed and are
described in the following. Figure 23 shows a group of three precipitates
adjacent to each other. The corresponding diffraction patterns (correctly
oriented) show that the three precipitates are symmetry-equivalent vari-
ants of the above described orientation relationship. Particle a is
viewed in the $(\bar{1}11)$ orientation, b is in the (111) and c in the
$(1\bar{1}1)$ orientation as seen by comparison of their respective diffraction
patterns with figs. 19 and 20. The three precipitates are rotated 70.5°
with respect to each other, an arrangement which allows a reduction of

the total strain energy. At the stage of precipitation in fig. 23 the particles have lost coherency as evidenced by the presence of dislocations in the interfaces (see fig. 22.1). The above strain energy argument applies mainly to the stage before coherency loss, and it is most likely that it is at this earlier stage that the different (symmetry-equivalent) precipitate orientations are determined.

The wavy line structure in particle a , fig. 23,2 results from Moiré interference of the (110) and the (0002) reflections (arrowed in the diffraction pattern), identical to the structure shown earlier in fig. 14. In contrast to particle c which shows weak (straight) Moiré fringes (fig. 23,2) no (0001) superlattice spots of the ordered β-Ta$_2$C structure is found in a . If this is not a result of the small volume of particle a , compared to c , it must mean that a has not yet developed an ordered arrangement of carbon atoms and hence still possesses the α-Ta$_2$C structure (fig. 15a). In the absence of kinetic data on the α-β ordering transformation in Ta$_2$C , it is not possible to decide whether ordering can be suppressed by cooling from 1400°C at about 1° sec^{-1}.

Groups of precipitates like the one in fig. 23 were found frequently in both the slow cooled and the quench-aged material (see for example fig. 13) and are considered an important mechanism of strain accommodation during precipitation.

3.7 Twinning of the incoherent precipitates

While plastic deformation of the surrounding matrix is the major mechanism of accommodating transformation strains, a number of different defects were also observed in the precipitates. Figure 24 shows an example of twinning in a precipitate after slow cooling from 1400°C.

The twins are marked T in fig. 24a. The corresponding diffraction
pattern is shown in fig. 20c. The precipitate is viewed from a (111)
matrix orientation. Twin spots in the spot pattern are labelled T .
The $(\bar{1}101)$ spot is common to both twin related parts of the precipitate
and superimposes on the $(10\bar{1})$ matrix reflection. In a dark field image
with this triple reflection the matrix as well as the twins are simul-
taneously in diffracting condition (fig. 24b). In any other reflection,
only one of the twin related parts of the precipitate will be in Bragg
condition at a time. This is shown in fig. 24a where $g = (\bar{1}10)$. The
twin interfaces can now be seen to be the $(\bar{1}101)$ planes, i.e., the mirror
planes of the twinning operation. This is therefore an example of a
coherent twin boundary. The twinning elements are $n_1 = [1\bar{1}02]$ and
$K_1 = (\bar{1}101)$.

A twin plane of $K_1 = (\bar{1}101)$ is rather unusual for hexagonal
structures. Of the hexagonal metals, only Mg exhibits the twin system
observed here. It is not part of the three twin systems reported for
zirconium which has the same c/a ratio of 1.592 as $Ta_2C.$ [39] However,
profuse twinning of this type was found in V_3N precipitates in the
V_3N-V [41] system as well as in Nb_2N-Nb [42] and Ta_2N-Ta [42]. The twin-
ning elements in these systems are identical and their orientation rela-
tionships are of the same type as in the present system, differing by
only about 1° in the amount of misorientation between the close packed
directions $[11\bar{2}0]$ and $[1\bar{1}1]$. However, in those three systems twinning
is found in all precipitates with fairly regular spacing, whereas in
Ta_2C , twins are observed only rarely and are of irregular spacing.

3.8 Dislocations and antiphase boundaries in the incoherent precipitates

A type of defect more typical for the precipitates in the system under investigation are dislocations. Examples can be seen in figs. 24, 25 and 26. Of the two dislocations in fig. 24, one crosses the precipitate entirely, the shorter one goes from the interface to the surface. They are visible in both diffracting conditions, $g = (\bar{1}10)/(0\bar{1}10)$ and $g = (\bar{1}01)/(\bar{1}101)$, and can therefore not be pure c-dislocations of $b = \frac{1}{3}[0003]$ for which $g \cdot b$ would be zero in fig. 24a.

More information about the Burgers vector of the dislocations can be extracted from fig. 25. The looplike configuration and the single dislocation below it are out of contrast in $g = (10\bar{1}1)$, fig. 25a, and in contrast in $g = (\bar{1}101)$ and $g = (\bar{2}110)$, figs. 25d and e. This is again inconsistent with a pure c-dislocation, and agrees only with $b = \pm \frac{1}{3}[1\bar{2}10]$, $b = \pm \frac{1}{3}[\bar{2}113]$ or $b = \pm \frac{1}{3}[11\bar{2}3]$ of the conventional dislocations in hexagonal structures.[44]

Figure 26 shows dislocations in a precipitate when the basal planes are in diffracting condition, i.e., $g = (0002)$. This proves that these dislocations do have a c-component and cannot be of the type $\frac{1}{3}\langle11\bar{2}0\rangle$. If it is assumed that all dislocations are of the same type, the combined information of figs. 24, 25 and 26 determines their Burgers vectors to be of the $\frac{1}{3}\langle11\bar{2}3\rangle$ type. Without this assumption, it can still be concluded that dislocations with both c and a components appear in the precipitates.

Another frequently observed feature is the presence of planar defects as demonstrated in fig. 26. The dark field image taken with $g = (0001)$, a superlattice reflection of the ordered $\beta\text{-Ta}_2\text{C}$ structure, shows dark and bright fringes along the [0001] direction. They

invariably end at the dislocations. Such fringes could be due either to stacking faults or antiphase boundaries. Since they are in strong contrast in the (0001) superlattice reflection and show only residual contrast in a "matrix" (0002) reflection, they must be discontinuities only in the superlattice, i.e., antiphase boundaries. The boundary planes are apparently perpendicular to the basal plane. Considering the ordered arrangement of carbon atoms in the $\beta-Ta_2C$ structure (fig. 15b)[37], where every other close packed interstitial plane is occupied, it is clear that only a displacement in the c-direction can produce an antiphase boundary. Since the c-direction is contained in the plane of the faults they are conservative antiphase boundaries, the type which is produced predominantly by shear. This also explains why the faults end at dislocations. Whenever these faults were observed, they always had conservative character, see for example, fig. 29c.

Summarizing the defect structure within the precipitates, it consists of dislocations with both a and c components, conservative antiphase boundaries and, less frequently, twins. ' combination of these leads to a multitude of possibilities for the accommodation of transformation strains by the precipitate itself.

3.9 Precipitate morphology and interface with the matrix

For an investigation of the precipitate shape, the surface orientation of the thin foils used must be known. This makes a determination of the exact shape more involved than finding the orientation relationship. The shape of incoherent precipitates is determined not only by the strain energy (as for coherent particles) but also by the structure of the precipitate matrix interface. The morphology and interface structure of the large particles considered here vary within certain limits. In the

following, the features common to the precipitates in the late stage of
the transformation will be demonstrated.

All precipitates are short in the [0001] direction; they are rod
shaped with the long direction contained in the (0001) plane, see figs.
24-26, 29. The interface tends to follow the close packed {110} planes
of the matrix. This is shown in fig. 27 which pictures the precipitate-
matrix interface in a tilted beam lattice image of a very thin region
of the crystal (< 500 Å). The orientation is $(00\bar{1})$. The precipitate
crystal clearly shows the doubling of fringes due to the ordered arrange-
ment of carbon on the (0001) Ta_2C planes. The fringe spacings in the
matrix and the precipitate differ by 5.8% as measured by optical diffrac-
tion and microdensitometry. Within the limits of accuracy of the mea-
surements, this corresponds exactly to the equilibrium plane spacings
of (0002) and (110) planes. Except for the discontinuity in plane spac-
ing, the interface is continuous and straight, closely following the
close packed planes (see arrows). Since it is seen edge-on, there is
little contrast from the interface in this imaging mode. The interface
(Fresnel fringe) contrast increases at the expense of the lattice fringe
contrast of larger objective defocus and shows the marked position more
clearly.

Two lattice images of another such interface are shown in fig. 28a,b.
Again, it is viewed edge-on, but it is not a straight interface. The
orientation here is $(1\bar{1}\bar{1})$ (compare with fig. 19 and 20a and d). At low
magnification, this appears to be a curved interface making an angle
with the close packed planes. That this curvature is made up of segments
along close packed {110} planes is clearly visible in the lattice fringe
images of (110)/(0002) and (101) planes in fig. 28 left and right. In

the short segments following the (101) planes, the (110) and (0001)
planes make an angle of 60° with the interface, see A and B. Thus the
5.8% mismatch between these two planes has to be accommodated in these
short segments. Burgers circuits drawn around these segments in the
left part of fig. 28 indeed show closure failures of one and two (110)
planes at B and A respectively. This proves that dislocations are pre-
sent in the interface, but does not determine their Burgers vector
uniquely.

Figure 25a,b,c shows a conventional analysis of the interface dis-
locations in a foil of $(0\bar{1}0)$ orientation. Although it was not shown for
this particular precipitate, it can be concluded from its large inclina-
tion and its trace along [001] that it lies on, or close to an (0001)/(110)
plane. (The (0001)/(110) and the $(0\bar{1}0)$ great circles intersect in the
$[00\bar{1}]$ direction in fig. 19.) This interface in fig. 25c shows a regular
array of straight dislocations along $[1\bar{1}2]$ in the (110) plane. They are
out of contrast in fig. 25a and b in $\underset{\sim}{g} = (\bar{1}01)$ and $\underset{\sim}{g} = (10\bar{1}1)$. This
means that

a) They are lattice dislocations since they disappear in a
precipitate reflection almost parallel to the $(\bar{1}0\bar{1})$ matrix
reflection for which $\underset{\sim}{g} \cdot \underset{\sim}{b} \neq 0$ (fig. 25a and c);

b) Their Burgers vector is $\pm \frac{1}{2} [1\bar{1}1]$ or $\pm \frac{1}{2} [111]$ since
for $\underset{\sim}{g} = (\bar{1}01)$, $\underset{\sim}{g} \cdot \underset{\sim}{b} = 0$, (fig. 25b).

c) Lying along $[1\bar{1}2]$ directions, the dislocations have mixed
character.

Another set of dislocations in the same interface is in contrast in $g = (\overline{1}01)$, fig. 25b, and out of contrast in $g = (\overline{1}0\overline{1})$, fig. 25c. They are more widely spaced and follow irregular directions. Their Burgers vector is $\pm \frac{1}{2}[11\overline{1}]$ or $\pm \frac{1}{2}[\overline{1}11]$. A network of these two sets of dislocations in the (110)/(0001) interface can produce a resulting shear in $\pm[110]$, $\pm[011]$, $\pm[100]$, or $\pm[001]$, of which only the last one is contained in the plane of the interface. The (001) planes are within a few degrees from being parallel to the $(11\overline{2}0)$ planes. Their relative mismatch is 6%. An array of dislocations with Burgers vector [001] spaced 130 Å apart would accommodate this mismatch. This estimate is in good agreement with the observed spacings of ~100-200 Å. It can be concluded that the structural mismatch in the long (110)/(0001) interface is completely accommodated by dislocation networks contained in the matrix side of the interface.

The same principle applies to the short interface, perpendicular to the (0001) planes. Here the mismatch is taken up by a single array of $\frac{1}{2} \langle 111 \rangle$ matrix dislocations. This is illustrated in fig. 29, in an $(0\overline{1}0)$ orientation. The short interface in Figs. 29b and c shows fairly straight evenly spaced dislocations (arrowed). They disappear in $g = (10\overline{1})$ and $g = (1\overline{1}0)$ and are visible in $g = (011)$ and $g = (110)$ and are therefore $\pm \frac{1}{2}[111]$ matrix dislocations. The irregular background structure in fig. 29a and d is believed to be due to Moiré interference. The spacing of these straight dislocations was found to be about 50 Å in all cases investigated. Figure 30 shows an example of the structure of the short interface with the same line spacing of about 50 Å, at high resolution. The superlattice fringe spacing in the precipitate is $d_{0001} = 4.95$ Å while the matrix spacing is $d_{110} = 2.34$

(2 d_{110} = 4.67 Å). The mismatch of 5.8% is completely accommodated by
an array of dislocations with Burgers vector $\pm \frac{1}{2}$ [111] spaced 1 (110)
planes apart $\left(\frac{100}{18}= 5.6\%\right)$. This is exactly the spacing of the optically
dense areas in fig. 30, as indicated by arrows on every 18th plane. It
is therefore concluded that the lines represent dislocations of Burgers
vector $\frac{1}{2}$ [111] in an inclined interface, and that their spacing is the
equilibrium spacing necessary for an accommodation of the 5.8% mismatch
betwe .. (0002) and (110) planes.

Figure 31 is an enlarged view of fig. 30 and shows how the misori-
entation of 1.5° between (0001) and (110) can be measured directly from
the micrograph. The inset diffraction pattern shows that the orienta-
tion is near ($1\bar{1}1$) (see also figs. 19, 20). The fringe spacings measured
in matrix and precipitate correspond again to the equilibrium plane
spacings for the two structures. Also note the variation of matrix and
superlattice fringe visibility with changing thickness in the precipitate.
This is a result of the three-beam situation for the lattice image of
the precipitate.[27,28]

3.10 Summary of results on carbon precipitation

The precipitation of carbon from supersaturated solution in tantalum
has been shown to proceed via the homogeneous nucleation of small meta-
stable coherent precipitates on {310} matrix planes. The platelike pre-
cipitates grow during ageing and lose coherency by plastic deformation
of the matrix. The structure of the final incoherent product is that
of ordered β-Ta_2C . The orientation relationship between the particles
and the matrix is ($\bar{1}101$) ∥ ($10\bar{1}$) and [$11\bar{2}0$]∥[$26,\overline{25},26$] . The defect
structure within the precipitates consists of twins with K_1 = ($\bar{1}101$)
and η_1 = [$1\bar{1}02$] , dislocations with both c and a components, and

conservative antiphase boundaries. The precipitates are rod-shaped
with a short direction along [0001]. The particle-matrix interface
tends to follow close packed planes of the matrix, and the misfit dis-
locations of Burgers vector $\frac{1}{2}$ $\langle 111 \rangle$ are entirely contained within the
matrix. The sequence of precipitation is very similar to the ones
reported for V-C[29] and Nb-C[32] alloys.

The most important finding is that by analyzing the metastable
coherent precipitates as dislocation loops, a vacancy-carbon co-
precipitation mechanism must be postulated.

4.   Experimental Results II - Interstitial Phases Resulting from Contamination

Prior to the experiments detailed in the preceding section, a num-
ber of control experiments designed to ensure the reproducibility of the
experimental results were done. This was a necessary and important part
of the present study since earlier reports of phase transformations in
the Ta-C system were rather contradictory. As the results in the fol-
lowing sections will show, contamination by both hydrogen and oxygen
does occur and can in fact explain all of the previously published
microstructural work on tantalum-carbon. The sources and mechanisms of
contamination of these two interstitial species are as different as the
resulting microstructures. Therefore the two systems will be treated
separately.

As mentioned before in the introduction, the following two sections
are only related to phase transformations in tantalum-carbon alloys inso-
far as they clarify the controversies of earlier research on this system,
and separate the artifacts introduced by hydrogen and oxygen contamination.
Since both, the hydrides and the suboxides of tantalum have recently
received increased attention in the literature, this report is limited
to those results which are new and pertinent to the understanding of
past and present work on the carbon alloys of tantalum. The following
two sections also provide a short description of the experimental tech-
nique as well as a limited discussion of the presented results. They
are thus self-contained and may be read separately, if desired.

4.1 Hydrogen contamination

In the majority of the work published on the microstructure of
dilute tantalum-carbon alloys a chemical polishing solution consisting

of HF and HNO_3 in a volume ratio of about 1:3 was employed to pre-
pare thin foils for electron microscopy[1-5]. Before using this tech-
nique on the carbon doped tantalum, samples of pure tantalum were thinned
in this chemical solution in search for possible artifacts introduced
by the thinning process.

The result of such a control experiment is shown in fig. 32. A
domainlike microstructure has formed with planar boundaries separating
domains of different contrast. The contrast behavior of these boundaries
is characterized by the top two micrographs in fig. 32. The fringe
contrast is asymmetric in bright field, i.e., top and bottom fringes
are of opposite color, and symmetric in dark field. The two micrographs
on the bottom show that the asymmetric profile obtained in bright field
is reversed when g is reversed. The color of the background changes
abruptly from one side of the boundary to the other. This indicates a
change in the deviation parameter s, i.e., a small rotation of the
diffracting planes. Such contrast behavior is typical of δ-fringes (or
mixed $\delta+\alpha$-fringes), occurring in structures that have suffered a small
distortion due to ordering. The observed boundary contrast is due to a
small change of extinction distance and orientation across the boundaries
and has been described in detail by Gevers et al.[45].

The crystal structure of the three domains separated by the boun-
daries in fig. 32 were determined by high angle tilting and selected
area diffraction, as shown in fig. 33. The foil was tilted around the
$[1\bar{1}0]$ axis through an angle of 70.5 degrees from the (111) to the $(11\bar{1})$
orientation. Each column in fig. 33 represents the diffraction patterns
of these three orientations for one of the domains. The one on the left
shows extra spots at $\frac{1}{2}$ $[0\bar{1}\bar{1}]$ positions, the center one at $\frac{1}{2}$ [011] and
the one on the right at $\frac{1}{2}$ [101].

An analysis of these single domain patterns leads to a reciprocal lattice as shown in fig. 34, top. The large circles represent the regular bcc matrix spots and the small circles are the observed extra spots at $\frac{1}{2}$ ⟨110⟩ positions. The figure shows only one of the six possible arrangement of extra spots. Using the method of static concentration waves devised by A. G. Khachaturyan,[46] the corresponding real space lattice was derived as shown in the bottom drawing of fig. 34. The outlined structure represents four unit cells in one of the nine independent sublattices made up of the tetrahedral and octahedral interstitial sites available in the body centered structure of tantalum. The tantalum atoms are not shown. They occupy a body centered lattice shifted by $\frac{1}{2}$ ⟨100⟩ or $\frac{1}{4}$ ⟨210⟩ with respect to the outlined sublattice. Occupied sites in the interstitial sublattice are marked by full circles. It can be seen that the interstitial atoms form a layer lattice with every other {110} plane occupied. This explains the appearance of superlattice diffraction spots at $\frac{1}{2}$ {110} positions as well as the fact that six different symmetry equivalent options are available for the formation of this structure from the disordered solid solution. However, from this diffraction information alone, it is impossible to determine on which of the nine interstitial sublattices the contaminating species is located. This is a direct result of double diffraction masking the true diffracted intensities as well as the low scattering power of the low-Z elements (H,O,N and C) to be considered here.

By comparison with the literature on interstitially ordered structures of tantalum it becomes clear that the contaminant is hydrogen, since only hydrogen orders in the observed layer lattice.[47,48] This β-Ta$_2$H phase is stable over a wide range of compositions. Nevertheless,

at least 20 at.-% hydrogen must have been introduced locally during the process of chemical polishing.

From earlier neutron diffraction data, it has been concluded that hydrogen prefers the tetrahedral interstitial sites.[47] It has further been reported that the tantalum host lattice suffers an orthorhombic distortion[48] and that the ordered layer lattice of the hydride causes a small periodic displacement of {110} planes of the tantalum lattice.[47] This displacement which has the same period as the hydrogen superlattice explains the high intensity of the observed superlattice diffraction spots (fig. 33), which would be impossible to account for in terms of electron scattering by the hydrogen alone.

The consequence of the orthorhombic distortion of the host lattice can be understood with the aid of fig. 35. The real space lattice of fig. 34 is here projected with the hydrogen layers viewed edge-on (here onto the (001) plane). Large circles indicate tantalum, small circles hydrogen atoms. The ordering of hydrogen is such that every other inter-stitial ($1\bar{1}0$) plane is occupied. Electron diffraction from the six structures shown in fig. 35[47] would be identical. All six arrangements cause a periodic displacement of ($1\bar{1}0$) matrix planes as shown schemati-cally in fig. 35a (arrows). The difference lies in the particular tetrahedral sublattice occupied. The z-coordinate of the hydrogen atoms is denoted by the filled fractions of the circles (for example, ◗ is a hydrogen atom at $z = \frac{1}{4}$). The body centered tantalum atoms ($z = \frac{1}{2}$) are marked by a horizontal cross line. The tetragonal symmetry of the tetrahedral interstices has its major axis along [001] in fig. 35a and b, [100] in 35c and d, and [010] in 35e and f. Since the orthorhombic distortion of the host lattice in the [$1\bar{1}0$] and the [001] directions

has its major axis along [001] (+2%), while [100] and [010] both suffer an elongation of only ~0.8%[48], only those two sublattices are expected to be occupied whose sites have their axis of tetragonality along [001]. Hence only the arrangements of fig. 35a and b are plausible ones.

These two structures are related by a mirror operation and are thus enantiomorphic to each other. They are energetically equivalent because they are related by a symmetry operation of the (distorted) host lattice. An attempt to reveal the presence of enantiomorphic domains in a high voltage electron microscope using the technique of van der Biest and Thomas[51], failed to give a contrast variation. However, this was to be expected since the major contribution to the diffracted intensity comes from the periodic displacement of the host atoms. In contrast to the position of the hydrogen atoms, this displacement is centrosymmetric, and identical for the two structures shown in fig. 35a and b. Thus, while it is impossible to rule out any of the six sublattices by means of electron microscopy alone, their number can be reduced to two by symmetry arguments. Since the two are energetically equivalent, no further distinctions can be made here.

Two orientations of this structure are shown in perspective in fig. 36. The orthorhombic unit cell of the distorted host lattice is outlined. Including both the distortion and the positions of hydrogen atoms, the symmetry of this structure is reduced to monoclinic even though the axes are at right angles, a point often overlooked in the literature.

Because of the symmetry of the bcc lattice there are six equivalent ways to form an ordered hydride lattice from a disordered solid solution, according to the six equivalent ⟨110⟩ directions. Each of these options leads to a different orientation of the orthorhombic distortion of the bcc lattice. The misorientation of the direction of

ordering between two ordered domains in the same crystal can only be 90° or 60° (according to the two possible angles between (110) directions). Any two such domains are related by a mirror symmetry operation. For 90° domains, these mirror planes are {100} planes, 60° domains are related by {110} mirror planes. If a domain boundary lies on the mirror plane that connects the two orientations, it is called a coherent twin boundary of the ordered structure.

{110} and {100} planes were indeed found to be the preferred orientations of domain boundaries, although small deviations were found. An example for a 90° boundary is given in fig. 32 where the boundary separating the center domain from the one on the bottom left is seen to lie close to the (100) plane (here seen edge-on). The direction of ordering changes from $[0\bar{1}\bar{1}]$ to $[011]$ across this boundary.

Figure 37 shows an example of some 60° domain boundaries. The contrast experiment in the last five of the micrographs in fig. 37 shows, among a number of other features, a coherent twin boundary (nearly vertical in the pictures) between the two 60° domains on the left and the right. The boundary is located on the $(1\bar{1}0)$ plane, separating domains with ordering directions $[011]$ and $[101]$. The unit cells of the two domains are shown in their relative orientation in fig. 36. Clearly, the $(1\bar{1}0)$ plane is the mirror symmetry plane between these two structures.

Using this particular (60°) coherent boundary as an example, a frequently observed phenomenon can be explained: domain boundaries like the ones shown in figs. 32 and 37 were often found to form platelike structures like the one in the top left micrograph of fig. 37. These plates are highly mobile during observation in the electron microscope, sweeping rapidly across the field of view upon focussing, and retracting

upon defocussing of the beam. The fact that this motion is rapid and reversible excludes diffusion as a possible explanation. The arrows in the first micrograph if fig. 37 show how a forward motion of the plates is accomplished by propagation of the domain boundaries in a direction perpendicular to the boundary planes.

The atomic rearrangements necessary for such a domain boundary motion are demonstrated in fig. 38. Here, the two structures shown in perspective in fig. 36, are projected onto the (001) plane. The (rectangular) projections of the two orthorhombically distorted unit cells are marked by thick solid lines. Only the positions of the hydrogen atoms are given with the same notation for their z-coordinates as used before, i.e. ◐ denotes $z = \frac{1}{4}$ etc. Note that z refers to the ordered unit cell, i.e., $z = \frac{1}{4}$ corresponds to $z = \frac{1}{2}$ in the disordered structure. The mirror plane between the structure at the top and the one at the bottom (coherent twin boundary) is the $(1\bar{1}0)$ plane, seen edge-on in this projection, parallel to the arrows. For the propagation of this boundary perpendicular to itself (i.e., perpendicular to the arrows) a twinning shear of only the hydrogen sublattice is required. The tantalum host atoms retain their positions except for a small distortion due to the reorientation of the direction of ordering. The arrows show how this twinning shear of the hydrogen sublattice can be accomplished by elementary cooperative jumps of the hydrogen atoms in $(1\bar{1}0)$ planes. The upper arrow indicates a jump of $\frac{1}{4}$ $[\bar{1}12]$, the lower arrow a jump of $\frac{1}{4}$ $[\bar{1}1\bar{2}]$. Carrying out these operations in successive $(1\bar{1}0)$ mirror planes will transform the upper structure into the lower one. With the extremely high diffusivity of hydrogen in tantalum (on the order of 10^{12} jumps sec^{-1} at room temperature[52]), such cooperative jumps can be accomplished

readily and can account for an advance of the domain boundary over several
thousand atomic distances within a small fraction of a second. The
driving force is the stress field induced by thermal expansion of the
foil under the action of the electron beam. This explains the observed
reversibility of the process. Therefore the proposed phase transforma-
tion cannot be classified as a thermally activated transformation. But
although the overall change accomplished can be described geometrically
by a twinning operation involving a large shear of both the tantalum and
the hydrogen atoms, the actual atomic rearrangements are minor, leaving
the tantalum host atoms virtually unmoved while the hydrogen atoms undergo
a reshuffle. Because of the small shape change of the transformed region
and the absence of long range diffusion, the transformation is best clas-
sified as martensitic.[33]

Mobile domain boundaries like the ones described above have been
reported in a number of publications on interstitial alloys of tantalum.
Hull and Wyne[53] gave a qualitatively similar explanation of their obser-
vation of domain boundary motion in hydrided tantalum foils. Stals and
van Landuyt[54] suggested that internal oxidation was the cause of order-
ing and mobile domain boundaries in tantalum (as well as in niobium[55]).
The same domain boundaries were found in the three major studies on the
$Ta_{64}C$ phase in alloys of nominal composition Ta-1.54 at.-%C[1],
Ta-2.05 at.-%C[5], and Ta-0.47 at.-%C[6] and were explained there in
terms of coherent domain boundaries in the ordered $Ta_{64}C$ structure.

The factor common to all these studies is that a strong acid
($HF+HNO_3$ or $HF+H_2SO_4$) was used to prepare thin foils for electron
microscopy. As shown in the control experiments above, this can lead
to the local introduction of large concentrations of hydrogen into the

tantalum foil. In contrast, Abe et al.[56] found that chemical polishing of bulk tantalum in $HF + HNO_3$ at room temperature introduces less than 0.002 at.-% hydrogen. However, since the absorption of hydrogen during chemical polishing is a surface phenomenon, the concentrations in the thin electron transparent part of a tantalum foil are expected to be very much higher.

That this is the case even though it may not be apparent under normal operating conditions of the electron microscope, is shown in fig. 39. The polishing solution, $(HF + HNO_3)$, was cooled to 0°C during the foil preparation. No ordering was found at room temperature as shown in the row of three diffraction patterns at the top of fig. 39. If ordering of hydrogen in any of the six (110) directions had occurred, it would have produced extra spots in at least one of the three orientations. After cooling the foil in situ to liquid nitrogen temperature, precipitates like the one shown in the two micrographs in fig. 39 formed. As seen in the central diffraction pattern, precipitation leads to the extra spots and spot splitting (see arrows) typical for the hydride. The precipitate redissolved at a temperature of -30°C, leaving an undistorted matrix diffraction pattern with no extra spots (bottom spot pattern).

Using the well-established solubility data for H in Ta[49,50], this solution temperature corresponds to a hydrogen concentration of ~8 at.-%. With this technique, local concentrations of hydrogen in thin tantalum foils can thus be measured accurately and in situ.

As a result of these control experiments, it is concluded that the absorption of hydrogen during thin foil preparation was responsible for some of the domain structures reported in the references quoted above. In particular, the mobile boundaries observed in the work on dilute tantalum-carbon alloys[1,5,6] are due to hydrogen contamination and not to carbon.

4.2 Oxygen contamination

The control experiments described in this section will show that all the previously published work on the ordered subcarbide $Ta_{64}C^{1-6)}$ can be explained as resulting from a source of contamination different from the one shown above. The phase previously identified as $Ta_{64}C$ is actually $Ta_{12}O$ and arises from the inadvertent introduction of oxygen into the tantalum during the heat treatments.

This conclusion is supported by the result that when all diffraction and contrast effects published in the literature are re-examined in the light of the present work, they can be explained consistently with the ordered suboxide $Ta_{12}O$, recently identified by Milillo and Potter.[17] This must mean that enough oxygen can be absorbed by the material under the given experimental conditions. The equilibrium carbide Ta_2C was not found in previous investigations because of its preferential attack by the chemical solution used to prepare electron transparent foils.

Figure 40 shows the tantalum rich side of the tantalum-carbon phase diagram.[57] The solution temperatures of the three major studies of $Ta_{64}C^{2,5,6)}$ are marked. Note that most of the heat treatments are in the two phase $\alpha+Ta_2C$ field, where extensive precipitation of the equilibrium Ta_2C phase is possible.

Reproducing the experimental procedure of the work of Rao and Thomas[5] but using a different polishing technique for making thin foils for electron microscopy in the final step, produced the expected Ta_2C precipitates, fig. 41a. This foil was electro-jet-polished in a solution of 4 vol-% H_2SO_4 in methanol at -30°C and a current density of 1A cm^{-2}. When such a foil was re-polished in the chemical solution employed by previous researchers (25 vol-% HF in HNO_3) the carbide precipitates were

preferentially etched, leaving holes of similar size and distribution, fig. 41b. This result is borne out by the findings of Kopyleva[58] who reports that tantalum carbide, although insoluble in most acids, will dissolve in a mixture of HF and HNO_3 .

While the absence of the equilibrium carbide precipitates in the work on $Ta_{64}C$ is explained by the particular polishing technique used, the observed diffraction and contrast effects are due to a different artifact. In all cases, the alloys were prepared by evaporating thin layers of carbon onto pure tantalum sheets followed by a diffusion anneal at temperatures between 1000 and 2000°C (fig. 40) in a vacuum of about 10^{-6} torr. Annealing times were between 2 and 48 hours. Under these experimental conditions, the following reactions have to be considered[59-63].

$$
\begin{array}{lll}
(1) & \frac{1}{2} O_2 \ (g) & \rightleftharpoons O \ (in \ \alpha) \\
(2) & H_2O \ (g) & \rightleftharpoons O \ (in \ \alpha) + H_2 \ (g)
\end{array} \left.\right\} \text{absorption of oxygen}
$$

$$
\begin{array}{lll}
(3) & C + O & \rightleftharpoons CO \ (g) & \text{decarburization} \\
(4) & mTa(s) + O \ (in \ \alpha) \rightarrow Ta_mO \ (g) & & \begin{array}{l}\text{material loss through}\\ \text{volatile oxides}\end{array}
\end{array}
$$
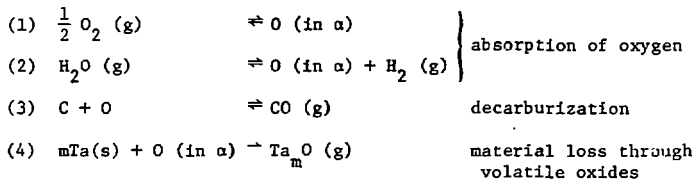
While (4) is of importance only at temperatures above $1700°C$[60] and can usually be neglected in comparison with the other reactions, (1), (2) and (3) can be quite rapid. According to the data of Jehn and Hörz[60], 0.1 mm sheets of tantalum can absorb 1 at.-% oxygen from an oxygen atmosphere at 10^{-6} torr in 3 hours at 1700°C by reaction (1). In water vapor (reaction (2)), the same amount is absorbed in 9 hours (at $PH_2O = 10^{-6}$ torr and 1700°C). The evaporated carbon film will initially react with residual gases at the vacuum/carbon interface and dissolve in the tantalum at the Ta/C interface. After the carbon layer has thus been

removed, the oxygen that is absorbed on the surface will then either go into solution according to reactions (1) and (2), or react with the dissolved carbon to form CO (reaction (3)). Since the latter reaction is controlled by the slow (relative to oxygen) diffusion of carbon to the tantalum surface, the solution of oxygen will be faster. The kinetics for oxygen absorption cited above will thus be upper limits for the given conditions. Even though the actual process may be more involved, and depend on the pressure and composition of the residual gases as well as the temperatures, these arguments show that appreciable absorption of oxygen, on the order of 1 at.-%, is to be expected under the experimental conditions of the work published on $Ta_{64}C$.

Such concentrations of oxygen have been known to be sufficient for the precipitation of the suboxides TaO_x or TaO_y formed at low aging temperatures.[12] In a careful analysis, Milillo and Potter[17] recently identified this suboxide as the ordered phase $Ta_{12}O$.

The morphology and diffraction patterns found for $Ta_{12}O$ are identical to the ones reported by Seetharaman et al.,[6] . Compare for example the microstructure in (fig. 2(d), Ref. 17) with the one in (fig. 4, Ref. 5). Both micrographs show large platelike precipitates on {100} planes of the matrix with regular internal twinning at a spacing of about 500 Å. The corresponding diffraction patterns (fig. 7(f) in Ref. 17 and fig. 5 in Ref. 6) reproduced in fig. 42d and e are identical. Superlattice diffraction spots at $\frac{1}{4}$ ⟨110⟩ positions appear in two of the three ⟨110⟩ directions, according to the two twin related parts of the precipitates. The diffusion anneal was similar in both cases. Although much too short for long range diffusion of carbon $(\sqrt{D_C t}\big|_{1hr/300°} \approx 20$ Å) it was sufficient for oxygen $(\sqrt{D_O t}\big|_{1hr/300°C} \approx 5500$ Å). Under the assumption that these ordered precipitates are

$Ta_{64}C$, Seetharaman et al.,[6] estimate a carbon concentration of 0.4 to 1.0 at.-%. Replacing $Ta_{64}C$ with $Ta_{12}O$, a range of 2-5 at.-% oxygen is obtained. This agrees well with the oxygen concentration of ~3.5 at.-% in Ref. 17. On the basis of this agreement, the diffusion kinetics, and the previous arguments, it is concluded, that the observed precipitate phase was $Ta_{12}O$ rather than $Ta_{64}C$.

While in Ref. 6, the solution treatments were near the solubility limit, in the case of Ref. 1, all heat treatments were far into the two phase field $\alpha + Ta_2C$ (fig. 40). After a 1 to 2 day anneal at 1000 to 1500°C, the equilibrium carbon concentration was most likely established. According to Ref. 57 these equilibrium concentrations are 0.3 at.-% at 1500°C and 0.09 at.-% at 1000°C (compared to 1.54 and 2.94 at.0% claimed in the study). Therefore, carbon could not have caused the observed diffraction and contrast effects, which are again identical to the ones in $Ta_{12}O$[17] - compare Ref. 17, figs. 2(d) and 7(a) with Ref. 1, figs. 4 and 6. Again note the twins on {110} planes and the systematic absence of the $\frac{1}{2}$ (800) spots in the diffraction patterns in both cases (diffraction patterns reproduced in fig. 42b and c). The ordering transformation is reported to occur by beam heating in the electron microscope, an effect which is incompatible with the low diffusivity of carbon, but quite possible for oxygen - as observed in the case of Nb by Van Torne and Thomas.[64] The same argument applies to Ref. 3 where similar microstructures and superlattice reflections are obtained by electron beam heating of evaporated tantalum films (Ref. 3, fig. 5). The author estimates the original oxygen concentration to be below 0.5 at.-% and concludes that the impurities responsible for the superlattice formation originate either in the surface oxide film or the microscope atmosphere.

The microstructures reported by Rao and Thomas[5] are less developed than in the other studies of "$Ta_{64}C$", although the observed superlattice is the same, see diffraction patterns reproduced in fig. 42a and c. They were obtained by slow cooling ($10°C \ min^{-1}$) from 2000°C in alloys of nominal carbon concentrations of 0.76 to 2.05 at.-%. The solubility limit at 2000°C is 1.27 at.-%. In agreement with Hörz et al.,[65] our results indicate that no more than 0.3 to 0.5 at.-% carbon can be held in solution even at much higher quenching rates of 700 to 2500°C sec^{-1}. Again, it seems clear that not carbon but oxygen was responsible for these microstructures. In fact, the small ordered precipitates of the 1.53 at.-% carbon alloy in Ref. 5, fig. 10, are identical in shape (square), size (1000 Å) and distribution, (but 45° rotated) to the ones found in Ta − 3.3 at.-% oxygen aged 1 hr. at 270°C, Ref. 17, fig. 2(b). It appears that continuous cooling at a rate of $10°C \ min^{-1}$ produces the same suboxide microstructures as a rapid quench followed by low temperature aging.

As a result of a detailed study of the literature on "$Ta_{64}C$", as well as the described experiments, it was shown that the carbon concentrations in the three major investigations of this phase[1,5,6] were too low to account for the observed effects. However these effects are found to be kinetically, thermodynamically and structurally consistent with the ordered $Ta_{12}O$ phase formed by oxygen contamination during the preparation of the alloys. The absence of the equilibrium carbide results from its preferential attack by the particular polishing solution. It can be concluded that the microstructure and phase transformations of a pure dilute tantalum-carbon alloy have never been studied prior to the present investigation.

5. Discussion

At first glance, the picture that presents itself for the time sequence of carbon precipitation from supersaturated solution in tantalum (as well as in Nb[31,32] and V[29,30]) is similar to some well known substitutional alloys (e.g., Al-Cu, Al-Ag, etc.)[33] with

(1) supersaturated solution

(2) metastable coherent precipitates (nucleated homogeneously)

(3) stable incoherent precipitates (ordered crystal structure)

However, a closer look reveals some fundamental differences. In Al-Cu, the metastable precipitates of stage (2) are nucleated homogeneously, then followed by two further metastable phases before the equilibrium incoherent θ-Cu Al$_2$ phase forms. The sequence observed in the present system involves only one metastable phase. The equilibrium phase develops first coherently and loses coherency during coarsening. While in Al-Cu the kinetics are very much faster than expected from high temperature diffusivities, in Ta-C, no anomalous transformation rates were observed. The precipitate spacings after 4 hrs at $\sim$ 400° C and 17 hrs at $\sim$ 500° C are well below the average diffusion distances of carbon in tantalum ($\sqrt{D_c t}$ |(4 hrs 1400° C) $\approx$ 0.7 μm, $\sqrt{D_c t}$ |(17 hrs 1500° C) $\approx$ 9 μm), see figs. 3 and 10.

In the substitutional system Al-Cu, it has been suggested[79] that only a long-lived supersaturation of vacancies can explain the anomalous diffusion rates, whereas in the system under investigation here, a vacancy mechanism is the only means of explaining the intrinsic dislocation loop character of early precipitates. Because of its fundamental importance, this point warrants further discussion.

5.1 Co-precipitation and binding of vacancies and interstitials

The precipitation of the small metastable particles shown and analysed in figs. 3-8 is observed only after an extremely rapid quench from a high temperature followed by a low temperature anneal. As shown by fig. 1, the quenching rate is fast enough to keep the carbon in supersaturated solution. After aging for 4 hrs at $\sim 400^\circ$ C, the carbon precipitates in very small plates which are associated with a vacancy type strain field, as shown in the analysis of fig. 7. Since carbon atoms in tantalum occupy (octahedral) interstitial sites, they experience a compressive stress, a fact which applies equally to clusters of carbon atoms. The only apparent explanation for the opposite observation is the co-precipitation of carbon with another species of opposite effect, i.e., either small substitutional solute atoms or vacancies, as recently proposed by West macott and Perez[34] for fcc metals.

Such a mechanism requires a binding interaction between interstitial carbon and the other species. Binding effects between substitutional and interstitial alloying elements have been demonstrated in some elegant experiments reviewed by Jack.[66] By introducing nitrogen into binary substitutional alloys, (Fe-Mo, Fe-V etc.) at constant activity, these authors were able to produce a fine scale distribution of "zones" rich in substitutional solute and nitrogen. Interstitial-substitutional binding here is simply a result of the higher solubility of nitrogen in the solute than in the matrix, causing the nitrogen to cluster with the solute. Such zones are metastable and form on {100} matrix planes. As expected, they are associated with an interstitial type strain field in all cases investigated. The effect of constant activity aging at an intermediate temperature is to allow redistribution of the substitutional

solute by short range diffusion while the high diffusivity of the inter-
stitial nitrogen permits it to equilibrate with this metastable micro-
structure. The process is therefore controlled by the mobility of the
substitutional solute at the temperature of constant activity aging.

A somewhat different situation exists for the present system during
quench-aging. The mobilities of interstitial carbon and substitutional
tantalum lattice vacancies are comparable. The activation energy for
diffusion of both, carbon and vacancies is about 1.8 eV[19,67]. Thus
no equilibration of one with respect to a metastable distribution of the
other is to be expected. Instead, both species will diffuse at a
comparable rate, even if no binding is assumed during diffusion. How-
ever, the resulting microstructure is very similar to the case of
constant   activity   aging--a high density of homogeneously nucleated
mixed clusters (or precipitates) of (substitutional) vacancies and
interstitials.

The fundamental difference between the two metastable clustering
processes lies in the nature of (substitutional) vacancies as compared
to substitutional solute atoms. Three important questions arise from
this difference, namely

1. How does the presence of interstitial carbon affect the
    equilibrium concentration of vacancies at any given temperature?

2. How does a binding influence the mobility of either species?

3. What is the effect of the transition of the precipitates from
    a vacancy type strain field in the early stage to an inter-
    stitial type (compressive) strain field in the later
    stages?

5.2 The effect of binding on the concentration of vacancies

The first question raised above results from the fact that lattice
vacancies are equilibrium thermodynamic entities produced or absorbed
by sources or sinks existing in the lattice and stabilized by their en-
tropy contribution. This is in contrast to the behavior of solute atoms
whose concentration is fixed by the composition of the alloy. If a
binding exists between vacancies and interstitial carbon, the nature
of this binding is a critical factor in the resulting change of the
equilibrium vacancy concentration. Assuming a nearest neighbour con-
figuration of vacancy and interstitial, the vacancy concentration will
increase from

$$c_V^o = A \exp \left(- \frac{E^F}{kT}\right)$$

to

$$c_V = A \exp \left(- \frac{E_V^F}{kT}\right) \; (1 - nc_i + nc_i \exp \left(\frac{E_B}{kT}\right)) \qquad 68)$$

where E_V^F :   enthalpy of vacancy formation: (2.9 eV)[67]

   E_B :   binding energy

   c_i :   concentration of interstitials

   n :   number of interstices next to a vacancy (here 6)

   A :   preexponential factor; $\exp (5.45)$[67)]

The concentration of bound vacancy/interstitial pairs is thus

$$c_B = c_i \, A \, \left\{ \exp\left(\frac{-E_V^F + E_B}{kT}\right) \; - \; 6n \, \exp\left(\frac{-E_V^F}{kT}\right) \right\} \quad .$$

The ratio of vacancies stabilized by binding to an interstitial (con-
centration c_B) to free vacancies (concentration c^o) is therefore

$$\frac{c_B}{c_V^o} = \frac{nc_i}{1-nc_i} \; \exp\left(\frac{E_B}{kT}\right)$$

At the temperatures under consideration here ($\sim$ 2000K), this number is always on the order of the concentration of interstitials, c_i, and much smaller than one, even with a strong binding E_B. Hence the increase of the number of vacancies due to binding is negligible at equilibrium. However, it is has to be kept in mind that rapid quenching produces a non-equilibrium situation. A large supersaturation of dissolved carbon can be frozen in as shown in fig. 1. The hypothesis of co-precipitation of carbon and vacancies requires that also a high supersaturation of vacancies is present. As shown above, this cannot be explained by an increase in the number of vacancies due to binding. It must therefore be a kinetic phenomenon connected to the presence of interstitials.

5.3 The effect of binding on mobility

It is well known that even with extreme quenching rates, no appreciable supersaturation of vacancies can be frozen in pure bcc metals.[67] After Glaeser et al.[69] the maximum quenching rate allowed to retain the equilibrium vacancy concentration at any temperature T is

$$\frac{dT}{dt} \bigg|_{equ} = - \nu j \frac{k}{E_V^F} T^2 \exp\left(- \frac{E_V^M}{kT}\right).$$

where $\quad E_V^M$: migration energy of vacancies

$\qquad E_V^F$: formation energy of vacancies

$\qquad$ k : Boltzmann constant

$\qquad \nu$: characteristic frequency

$\qquad$ j : relative density of vacancy sinks.

For the grain sizes to be considered here, the relative density of vacancy sinks j is determined by the dislocation density ρ only. $j = 10^{-8}$ for a realistic dislocation density of $\rho = 10^7$ cm^{-2}. The values for E_V^M and E_V^F are 1.9 eV and 2.9 eV, respectively,[67] and $\nu = 10^{13}$ sec^{-1}.

With those data

$$\frac{dT}{dt} \Big|_{\substack{2100^o \ C \\ equ.}} = -1530^o \ C \ sec^{-1} \ .$$

The experimental value of 2500° C sec^{-1} is higher, so that a slight supersaturation can be expected. However, the following estimate shows that the expected supersaturation is negligible, even with much higher quenching rates.

The loss of vacancies during a quench can be approximated for small quench intervals and constant quench rate $\frac{1}{\alpha}$ as

$$(2) \qquad \ln \frac{c_V}{c_V^o} = - \ j \ \nu \ \alpha \ \exp \left(- \frac{E_V^M}{kT_o} \ \frac{\Delta T}{T_o} \right)$$

where c_V :   quenched-in concentration of vacancies

        c_V^o :   vacancy concentration at quench temperature T_o

It is clear from this estimate that even a quenching rate of $\frac{1}{\alpha} = 10,000^o$ C sec^{-1} will only produce a supersaturation ratio of

$$\frac{c_V}{c_V^o} \approx 1.2 \ x \ \frac{c_V^o \ |_T}{c_V^o \ |_{T_o}}$$

i.e., the quenched-in concentration will only be 20% higher than the equilibrium concentration at the same temperature. The experimental quench is thus too slow to account for the necessary supersaturation.

Equation (2) also shows that a change in the activation energy for migration has very little effect on $\dfrac{c_v}{c_v^o}$, and this effect would only concern the negligible fraction of vacancies which are bound to interstitials, as shown above.

5.4 A hypothesis for vacancy trapping

A solution to this dilemma presents itself in the following model. The rapid loss of vacancies during quenching can be assumed to stop abruptly when the solubility limit of interstitial carbon is reached. At this print, carbon tends to precipitate from solution. It is therefore reasonable to assume that the excess carbon now turns into effective trapping centers. The density of these trapping centers is several orders of magnitude higher than the sink density due to dislocations. Thus all vacancies present at this temperature are trapped immediately. The degree of clustering of these complexes during the remaining quench depends on their mobility, which is not very crucial at this stage of the analysis. Similarly the question of how many carbon atoms can be associated with one trapped vacancy is inconsequential. The important point is that most vacancies present at the temperature of the solubility limit T_i^S for the given carbon concentration are retained by trapping. This is a good assumption since a supersaturation of interstitials equal to the concentration of vacancies is reached within < 1°C undercooling below T_i^S.

Under the experimental conditions here, the solubility limit would have been reached at T = 1700° C. With Seeger's[67] values for the vacancy concentration, this corresponds to

$$c_v^o = 3.6 \times 10^{-6}$$

In comparison, the vacancy concentration necessary to explain the experimental evidence is estimated as follows: The observed loop density is $\sim 10^{15}$ cm^{-3}, the average loop radius ~ 100Å, the displacement vector $\sim \frac{1}{3} \langle 310 \rangle$, and the atom density in {310} planes 0.06Å^{-2}. A displacement vector of $\frac{1}{3} \langle 310 \rangle$ corresponds to the removal of three {310} planes. Thus, there must be $3 \times (100$Å$)^2 \times \pi \times 0.06$Å$^{-2} = 5.5 \times 10^3$ vacancies available per loop, or 5.5×10^{18} per cm^3. The required vacancy concentration is therefore $c_v = \dfrac{5.5 \times 10^{18}}{10^{24} \text{ Å}^3/v_{Ta}}$, where v_{Ta} is the volume of a tantalum atom. Hence,

$$c_v = 9.9 \times 10^{-5}.$$

This is 30 times more than the equilibrium value at the temperature of trapping (1700° C). While it is not in good agreement with the model, it is within the range of experimental error. The initial quenching rate may have been much higher, the carbon concentration may be higher than 0.5 at -%, the displacement vector could be smaller. All of these factors would lead to a better matching of experimental and calculated values, so that the model remains valid.

The proposed mechanism is also in agreement with the observation of large precipitate-free zones near grain boundaries, fig. 9, and hetero-geneous nucleation on dislocations, fig. 3, not visible at dislocations

in the as-quenched material, fig. 1. The precipitate-free dislocations in the as-quenched material show that dislocations do not continuously absorb trapped vacancies during the quench, since that would lead to climb of the dislocations, leaving behind precipitated carbon. The precipitates at the dislocations in the aged material (fig. 3) form only during aging, therefore only a small depleted zone ($\sim 500\text{\AA}$) is found around the dislocations.

In contrast, the precipitate-free zone at the grain boundaries (fig. 9), is much larger ($\sim 10,000\text{\AA}$). Assuming that all interstitials and vacancies from this zone are completely absorbed in the boundary, about 10 monolayers of carbon would precipitate. This is an upper limit, and a more realistic value is probably on the order of one monolayer since not all the carbon from the zone will go to the boundary. Hence no precipitates are expected to be seen in the boundary, in agreement with fig. 9.

The main conclusion that can be drawn from the existence of the depleted zone, in terms of the proposed mechanism is that trapping does not drastically decrease the mobility of either species. This is consistent with the conclusion of ref. 70 who postulate an increase in the mobility of vacancy/carbon complexes in bcc iron.

In summary then, the trapping mechanism proposed here is in agreement with all the experimental evidence presented. Its main feature is that it explains the fact that quench-aging experiments with pure bcc metals do not produce vacancy loops as with fcc metals. This is a natural result of the postulate that the amount of vacancies held in supersaturated solution depends on the temperature of supersaturation for the dissolved interstitials. The effect should therefore be most

pronounced for an interstitial alloy with a very low solubility for the interstitial, for example carbon in Mo or W. On the other hand, no co-precipitation effect should be observed for alloys with relatively high solubility like oxygen or nitrogen in tantalum, niobium or vanadium.

It is also clear that the quenching temperature should be unimportant as long as it lies above the solubility limit for the given concentration of interstitials. For a given system, the important parameter should be the concentration of interstitials. For a very low concentration as in pure metals, the interstitial saturation limit is only reached at temperatures where most vacancies have escaped.

While this predicted behavior is in agreement with experiments on bcc alloys, it stands in marked contrast to the expected behavior of fcc metal-interstitial alloys.[34] The co-precipitation of vacancies and interstitials in fcc-systems should depend strongly on the quenching temperature since it is known from pure fcc metals that both the rate and the temperature of a quench determine the final supersaturation of vacancies.

While it is obvious that a more detailed comparison of the different proposed mechanism would be interesting, the final answer can only be obtained from experimental evidence. It is therefore deferred to the last section where some of the most interesting future experiments are listed.

5.5 The effect of vacancy/interstitial co-precipitation on age-hardening

Of the three questions arising from the thermodynamic nature of vacancies as opposed to substitutional solute atoms, the last one has a bearing on the age-hardening behavior of the alloy. The experimental

analysis shows that the initial coherent precipitates have a vacancy strain field and that the later coherent precipitates, before the loss of coherency, have the hexagonal Ta_2C structure with larger atomic volume than the tantalum matrix. Thus the precipitates, in order to go from the early to the late coherent stage, must reach a point of no strain field. The growth sequence is therefore

    (1)   coherent vacancy-type precipitate →

    (2)   coherent strain free precipitate →

    (3)   coherent interstitial-type precipitate →

    (4)   incoherent precipitate

In each of the four stages, the precipitates will have a characteristic interaction with dislocations, leading to four distinct stages during age-hardening.

Stage (1) can be described as a fine distribution of partial edge dislocation loops, each associated with a cloud of carbon impurities.

Stage (2) corresponds to an array of strain free plates of high carbon concentration--similar to strain free GP zones.

Stage (3) is the well-known case of coherent precipitates with a large coherency strain field.

(Stage (4) is also well-known as the hardening effect of partially or completely incoherent precipitates.

Thus in Stage (1), the strength of the material will result from solid solution and pinned dislocation loop hardening. Stage (2) is a typical case of chemical hardening, effective only because of the thin plate shape and high density of the strain-free precipitates.[71] Stages (3) and (4) depend mainly on the strength and distribution of the precipitates.

No experiments have been reported as yet on the age hardening behavior of quenched dilute Ta-C alloys. However, Chang et al.[72] published results on the age hardening of V-C and Nb-C after rapid quenching. As mentioned before, both systems display a precipitation sequence identical to the one found here for Ta-C, although no analysis was made there of the loop nature of the early precipitates. It seems reasonable to expect the same carbon-vacancy co-precipitation mechanism in these two systems. Hence the age-hardening behavior of Ta-C can conversely be expected to be similar to Nb-C and V-C. The comparison is encouraging: Chang et al.[72] did indeed find four distinct hardness peaks during aging in both systems. By means of electron microscopy, they show that the first three stages all correspond to a microstructure of the well-known coherent plates on {310} planes. These authors did not find any qualitative difference between the three microstructures (except for the size of the coherent precipitates), and were therefore unable to explain the first two hardness peaks. A vacancy-carbon co-precipitation mechanism provides a natural explanation for the reported behavior as outlined above.

It is interesting to note that the same four-stage age-hardening sequence was found during the aging of cold rolled vanadium, super-saturated with carbon.[73] The high density of dislocations introduced by cold rolling had no effect on the type or kinetics of the "homogenous" nucleation of the {310} coherent precipitates. This observation is also consistent with the mechanism found in the present research.

No attempt is made here to provide a more detailed discussion of the possible hardening mechanisms although an analysis of this type of system should be extremely interesting because of the unusual trans-formation sequence. However, before turning to the later stages of the

transformation sequence, the possibility of introducing excess vacancies by means other than quenching will be discussed, namely dislocation climb and radiation damage.

5.6 The effect of vacancies produced by dislocation climb

If a tantalum sample contains a supersaturation of interstitials, but not enough vacancies to produce homogeneous metastable precipitates, vacancies given off by a climbing dislocation could provide the necessary partners for nucleation. Such a mechanism has been reported before by a number of workers (see for example ref. 38) who observed the precipitation of colonies of VC precipitates in the wake of a climbing a (100) edge dislocation in a low-carbon iron-vanadium alloy. A similar mechanism is suggested here for the secondary precipitation of carbon inside prismatic dislocation loops, see fig. 18. The material was slowly cooled from 1400° C, a process which allows extensive precipitation of the equilibrium carbide of hexagonal crystal structure, in which a tantalum atom takes up a volume about 15% larger than in the metal matrix. The growing precipitates thus loose coherency by punching out prismatic dislocation loops, as shown in figs. 16 and 17. Although not shown explicitly by experiment, the punched dislocation loops must have interstitial character, because of the volume increase during the transformation. The growth of these loops by outward climb can then both relieve increasing transformation stresses and provide vacancies on their inside which would make possible the "homogeneous" precipitation of carbon.

With a tantalum sample of carbon concentration 0.5 at -%, equilibrium carbide precipitation takes place at the "homogenization" temperature of 1400° C until the equilibrium carbon concentration of 0.15 at -% is

reached. During subsequent slow cooling, further carbon precipitation causes growth of the existing precipitates and (probably heterogeneous) nucleation of new carbide precipitates. While no supersaturation of vacancies can be maintained during cooling, it is possible that vacancies produced at low temperatures provide the necessary agent for the nucleation of homogeneous precipitates such as observed in fig. 18. The precipitates would naturally be inside the climbing prismatic loop, since vacancies are created only by an outward climb of the loop.

A test of this mechanism for homogeneous secondary nucleation would be provided by aging a tantalum sample containing a small concentration of carbon in solution, under creep conditions. The carbon concentration must be limited to small amounts in order to obtain a supersaturation of interstitials without simultaneously quenching in a supersaturation of trapped vacancies.

5.7 The effect of radiation produced vacancies

One of the most serious problems in structural nuclear materials is void swelling caused by the conglomeration of radiation produced vacancies. Although the controlling factors are at this point by no means well understood, there is evidence that interstitial impurities like carbon and oxygen lead to a strong increase in resistance to swelling.[74] This evidence has been discussed by Westmacott and Perez,[34] who pointed out that vacancy-carbon co-precipitation forming carbon saturated vacancy loops should lead to greater stability in an irradiation environment. This is equally valid for fcc and bcc metals and would be of special technological importance for the bcc refractory metals which are now under consideration for first wall applications in fusion reactors.

5.8 Loss of coherency

After the coherent precipitates grow to a certain size, coherency
stresses become too large, resulting in plastic deformation of the matrix.
The experimental evidence shows that one major mechanism is the punching
of dislocation loops in or near the particle matrix interface (for
example, fig. 16). As descussed by Viswanadham et al.[32] for the case
of coherency loss in the similar Nb-C system, the critical size pre-
dicted by the energy criterion of Brown et al.[75] and Ashby et al.,[76]
is much smaller than 500Å, the largest coherent carbide precipitates
observed here. Viswanadham et al. conclude that the coherent carbide
has a metastable bcc structure of small misfit and that loss of coherency
takes place instantaneously when the precipitates transform to their
equilibrium hexagonal structure. This conclusion cannot be confirmed
for the Ta-C system, because faint extra diffraction spots consistent
with the hexagonal carbide structure are found to arise from the large
coherent carbide particles (see fig. 11). Hence it must be concluded
that the equilibrium carbide precipitates can remain coherent up to a
size of at least 500Å.

When coherency is lost, a heavy deformation of the matrix takes
place. Fig. 13 is a graphic illustration of this deformation during
precipitation at 800° C. As in the case of mechanically deformed metals,[71]
dislocations are arranged in cell walls. While the present work only
outlines some principal features of the coherency loss, a more detailed
study could provide an interesting test of the various models proposed
in the literature.

5.9 Orientation relationship and morphology

The derivation of the orientation relationship between the hexagonal Ta_2C and the bcc matrix lattice has been described in detail. As pointed out before, it is almost identical to the ones observed in the V-N,[41] Nb-N[42] and Ta-N[42] systems and differs characteristically, though only by a small amount, from the ones reported for the V-C,[29] Nb-C[32] and W-C[43] systems. While all these orientation relationships are within a few degrees of the ideal Burgers relation, the morphologies of the precipitates vary drastically. It will be shown that these different morphologies, in particular the one found here for the Ta_2C precipitates, can be explained in terms of a simple model applied by Potter[41] to precipitates of V_3N in V. It follows from energetic considerations that planes of minimum mismatch will tend to be parallel--as far as possible within the proximity of the Burgers relation. If it is then assumed that growth of the precipitates is easiest in the directions normal to these planes of minimum mismatch, the shape of an unfaulted precipitate can be predicted. As pointed out by Potter, this is a reasonable assumption for two reasons: the stresses impeding growth are minimized in low mismatch directions and only small atomic rearrangements (shuffles) are necessary. In addition, the number of misfit dislocations in the interface between matrix and precipitate is small, resulting in particles of minimum interface energy.

In Table 2, the mismatch Δ of some low index planes which are approximately parallel in the orientation relationship is listed for a number of bcc – hexagonal precipitation systems. The indices used are the ones of the sterogram in fig. 19. Planes which are exactly parallel are marked by (*).

First, consider the Ta/Ta$_2$C system, column 1 in Table 2. The mismatch is a minimum (0.3%) in the direction perpendicular to $(1\bar{1}2) \mid (\bar{1}100)$, (the direction is written here as $[1\bar{1}2] \mid (\bar{1}100)$, keeping in mind that in hexagonal lattices, directions are not generally perpendicular to planes of the same indices). The $[1\bar{1}2] \mid (\bar{1}100)$ direction (best match) lies in the $(110) \mid (0001)$ plane (see stereogram, fig. 19). Within this plane, at 90° to the direction of best match, the mismatch takes on a maximum of 18.6% (in the $[1\bar{1}1] \mid [11\bar{2}0]$ direction, see Table 2). At 90° to both of these directions, in $[110] \mid [0001]$, the mismatch is also large, 5.8%. The precipitate will therefore be long only in the $[1\bar{1}2] \mid (\bar{1}100)$ direction (best match) and short in the two directions perpendicular to it, i.e., it will be rod or needle shaped. This is borne out by the experimental results presented earlier.

Turning now to the V$_3$N/V system in column 2 of Table 2, it can be seen that the main difference to the Ta$_2$C/Ta system, apart from small systematic differences in mismatch, is the fact that here, the direction of best match is $[10\bar{1}] \mid (\bar{1}101)$, (0.4%) at an angle of 30° from the direction of best match in Ta$_2$C/Ta. It should be noted that this direction is the plane normal of the twin planes in these systems. Profuse twinning is observed in V$_3$N[41] and tends to average out the mismatch perpendicular to both the twin plane normal (best match) and the $[1\bar{1}1] \mid [11\bar{2}0]$ direction (worst match, cf. Table 2 and fig. 19). Thus, due to twinning, the precipitates can be elongated in two directions, $[10\bar{1}] \mid (\bar{1}101)$ and $[121] \mid (1\bar{1}03)$. Hence the precipitate should be a platelet, in agreement with the experimental observations, as pointed out by Potter.[41]

From these two systems, one tentative empirical conclusion may be drawn that regular twinning is only observed when the twin plane normal

in the precipitate coincides with the direction of minimum mismatch. To test this conclusion, consider the other systems listed in Table 2. Only the two systems Ta_2N/Ta and Nb_2N/Nb (columns 3 and 4 of Table 2) display the same behavior as the V_3N/V system. Indeed, in both of these precipitation systems, extensive twinning and plate shaped precipitates are found.[42] The orientation relationship is also one with the twin plane exactly parallel to a close packed $(10\bar{1})$ bcc plane, as in the first two systems.

The remaining examples are similar to the Ta_2C/Ta system with the small but apparently important difference that (0002) and not $(\bar{1}101)$ is exactly parallel to a {110} bcc plane. No twinning has been reported in any of these systems.[24,32,43] The explanation clearly lies in symmetry considerations: It can easily be verified geometrically that twinning in a precipitate will in general create a new and less energetically favorable orientation relationship between the twin and the matrix. Thus twinning will be impeded under general circumstances. However, if for some special orientation relationship, the twin plane in the precipitate is <u>exactly</u> parallel to a matrix plane of the same (mirror) symmetry, twinning can occur without creating a new orientation relationship between the twins and the matrix. This special situation is realized when the $(\bar{1}101)$ twin plane is exactly parallel to the $(10\bar{1})$ matrix plane as in the case of Ta/Ta_2C, V/V_3N, Ta/Ta_2N and Nb/Nb_2N. As mentioned before, twinning has been observed in all of these systems, but not in any systems which do not fulfill the above requirements.

The same symmetry requirements apply to other planar defects, such as stacking faults. If a periodic arrangement of stacking faults on close packed (0001) planes of the precipitates creates a structure

which has the same symmetry as the {110} bcc matrix planes, then faulting
does not create a new orientation relationship as long as the fault
planes are exactly parallel to the {110} matrix planes. Heavy periodic
faulting along with the required $(0001) || (110)$ parallelism has indeed
been observed in the Nb/Nb_2C system.[42] Unfortunately, no report was
made of the morphology. However, with the argument developed above and
by comparison with Table 2, a platelike morphology is expected in which
the particles are elongated in the direction of best match $([1\bar{1}\bar{2}] | (\bar{1}100))$
as well as in one other direction for which the misfit is averaged out
by the periodic faulting. Future experiments in this and other systems
should provide an interesting test of this symmetry requirement.

In summary, it is remarkable that the simple model outlined by
Potter[41] is successful in explaining the fact that a very small degree
of variation ($\pm 3^{\circ}$ max.) in the orientation relationship results in a
radical change in morphology. It should be possible to calculate the
exact orientation relationship from the strain energy minimum in
anisotropic elasticity, and thus a prediction of precipitate morphologies
in a variety of technologically important systems like steels and β-titanium
alloys would become feasible.

5.10 Future Experiments

Resulting from the experimental evidence presented and in conjunction
with the models laid out in the discussion section, a number of experi-
ments will be outlined here.

The mechanism of vacancy carbon co-precipitation lends itself to a
variety of interesting tests. A study of the precipitation behavior of
a tantalum alloy supersaturated with carbon would be of great interest

in terms of the influence of interstitials on swelling under radiation conditions. With the vacancy-carbon binding established in the present research, void formation would be expected to be retarded due to the stability of carbon-trapped vacancy loops. Unfortunately, the 650kV high voltage electron microscope available at Berkeley does not allow an in situ study because of the high threshold energy for the displacement of tantalum atoms.

A highly interesting test of the proposed trapping mechanism could be performed on a number of different bcc-interstitial alloys. Using the Ta-C system, a simple test would be the comparison of the volume fraction of vacancy type precipitates formed after quenching from different temperatures and in alloys of different carbon concentration. It is predicted that the quenching temperature is unimportant, and that a high precipitate concentration should be obtained for high carbon concentrations ($\sim$0.5 at -%) and no vacancy-type precipitates are expected for low concentrations of carbon ($\sim$0.2%). This is opposite to the predicted behavior for fcc metal-interstitial systems. A still higher concentration of precipitates is expected for Mo-C alloys because of the lower solubility of Mo for carbon.

If the experiments confirm these predictions, they can be used to determine the enthalpy of formation of vacancies in these alloys. In addition, the width of depleted zones near grain boundaries might give some clues about the energy of migration of vacancy-interstitial complexes.[77]

No such effect would be expected for alloys of refractory metals with oxygen, nitrogen or hydrogen because of their high solubilities for these interstitial elements.

Both high resolution lattice imaging and convergent beam micro-diffraction analysis should be capable of giving more information about the structure of the metastable coherent carbide. The knowledge of this structure would be the clue to an understanding of the {310} habit of these precipitates.

Finally, the success of the energy criterion used to explain morphologies of incoherent hcp precipitates in a bcc matrix, makes further morphological studies in similar and other systems desirable. The ultimate goal here would be the capability to predict the shape of any incoherent precipitate in any matrix, for example transition metal carbides in steels. As can be seen from this brief list of possible future experiments, the present research has answered some questions and opened many others which will hopefully help in the understanding of metal-interstitial alloys in general.

6.   Summary and Conclusions

A detailed investigation of phase transformation in dilute tantalum-carbon alloys has led to the following significant results:

- dilute coherent ordered phases (as $Ta_{64}C$) do not exist in the binary tantalum carbon system.

- All previously published literature on $Ta_{64}C$ can be explained in terms of the inadvertent absorption of two interstitial con-taminants, namely

- oxygen, leading to the formation of the dilute ordered $Ta_{12}O$ phase, and

- hydrogen, leading to the observation of mobile domain boundaries in Ta_2H, for which a model is presented in this thesis.

- Oxygen contamination occurs during vacuum heat treatments.
- Hydrogen is absorbed during chemical thinning of foils for electron microscopy.
- Chemical thinning also causes preferential etching of the equilibrium carbide precipitates in Ta-C alloys.
- As a result of the effect of contamination on earlier work, the present research is the first microstructural study of phase transformations in tantalum-carbon alloys.

The results can be summarized as follows:

- A dislocation loop analysis of the metastable coherent precipitates leads to the formulation of a vacancy-carbon co-precipitation mechanism, consistent with all the evidence presented.

- A theoretical application of this result to age-hardening gives encouraging agreement with previously unexplained experimental results on other refractory metal-carbon systems.

- A vacancy-interstitial trapping mechanism is proposed capable of explaining quench-aging experiments in both pure and alloyed bcc metals.

- On the basis of the proposed mechanism, a number of experiments and applications is suggested including quench-aging, radiation damage and high resolution microscopy.

- The precipitates lose coherency during growth by loop punching as one major mechanism.

- The structure of the equilibrium carbide precipitates is the ordered hexagonal layer lattice of $\beta-Ta_2C$.

- The orientation relationship between matrix and precipitate structure is $(\bar{1}101)||(10\bar{1})$ and $[11\bar{2}0]||[25,\bar{2}\bar{6}, \bar{1}5]$.

- The defect structure of the precipitates consists of conservative antiphase boundaries, dislocations and occasional twins of $K_1 = (\bar{1}101)$ and $n_1 = [1\bar{1}02]$ type.

- The precipitate-matrix interface contains mismatch dislocations of Burgers vector $1/2 \langle 111 \rangle$ of the matrix.

- The interface tends to follow close packed matrix planes on a near-atomic scale.

- Precipitates are rod-shaped, elongated along the normal to the $(1\bar{1}\bar{2})||(\bar{1}100)$ planes of minimum mismatch.

- A minimum energy model for the growth of incoherent precipitates is successful in explaining vastly different morphologies in a number of bcc-hexagonal precipitation systems.

ACKNOWLEDGMENTS

I appreciate and acknowledge the stimulating environment provided by Professor G. Thomas and his group. I am particularly grateful to Dr. K. H. Westmacott whose kind advice and scientific enthusiasm were invaluable. My thanks are extended to T. M. Shaw, B. Chin, B. Drosd as well as Drs. R. Gronsky and R. K. Mishra for sharing their experience and knowledge in many discussions. I am indebted to Dr. W. Kriven for providing the computer plots of stereographic projections and, more importantly, for her active interest in this dissertation.

Although not directly involved in this work, the help and encouragement of Professors E. Hornbogen and H. Gleiter have been of much importance. The continuous moral support from my parents and friends has been more valuable to me than I can express. I would be at a loss if I tried to thank Penelope whose loving support, intelligent advice and constant companionship are but a small fraction of the many ways in which she has been important.

REFERENCES

1. R. E. Villagrana, G. Thomas. Appl. Phys. Lett. **6**, 61 (1965).

2. R. E. Villagrana, G. Thomas. Phys. Stat. Sol. **9**, 499 (1965).

3. R. B. Marcus. J. Appl. Phys. **37**, 3121 (1966).

4. P. Rao, G. Thomas. Scr. Met. **4**, 243 (1970).

5. P. Rao, G. Thomas. ACTA Met. **23**, 309 (1975).

6. V. Seetharaman, S. Banerjee, R. Krishnan. Phys. Stat. Sol. (a) **36**, 39 (1976).

7. J. W. Edington, R. E. Smallman. ACTA Met. **13**, 155 (1965).

8. G. Thomas, R. E. Villagrana. ACTA Met. **14**, 1633 (1966).

9. M. Cambini, M. Heerschap, R. Gevers. Mat. Res. Bull. **4**, 633 (1969).

10. M. Cambini, G. Pellegrini. Mat. Res. Bull. **6**, 791 (1971).

11. S. Steeb, J. Renner. J. Less-Comm. Met. **10**, 246 (1966).

12. J. Niebuhr. J. Less-Comm. Met. **10**, 312 (1966).

13. R. H. Geiss, K. R. Lawless. Proc. 26 Ann. EMSA Meeting, 428 (1968).

14. J. Van Landuyt, C. M. Wayman. ACTA Met. **16** 803 (1968).

15. M. P. Usikov, A. G. Khachaturyan. Sov. Phys. Cryst. **13**, 910 (1969).

16. N. Harris, A. Taylor, J. Stringer. ACTA Met. **21**, 1677 (1973).

17. F. F. Milillo, D. I. Potter. Met. Trans. **9A**, 283 (1978).

18. G. L. Miller. "Tantalum and Niobium." V. 6 of Metallurgy of the Rarer Metals. AC. Press, N.Y. (1959).

19. "Gase und Kohlenstoff in Metallen" E. Fromm, ed., Springer, Berlin (1976).

20. K. H. Westmacott, R. L. Peck. J. Phys. E: Scientific Instruments **9**, 521 (1976).

21. G. Hörz, R. Ziegeldorf. Z. Metallk. **68**, 16 (1977).

22. J. Mathuni, R. Kirchheim, E. Fromm. Z. Metallk. **69**, 277 (1978).

23. P. B. Hirsch, A. Howie, R. B. Nicholson, D. W. Pashley, M. J. Whelan. "Electron Microscopy of ·Thin Crystals." Butterworth, London (1965).

24. G. Thomas, W. Bell in "Lattice Defects and Their Interactions" ed. Hasiguti, Gordon & Breach Sci. Publ. Inc., N.Y. p. 477, (1967).

25. H. Föll, M. Wilkens. Phys. Stat. Sol. (a) 31, 519 (1975).

26. D. J. H. Cockayne. Z. Naturforsch. 27a, 452 (1972).

27. V. A. Phillips. "Modern Metallographic Techniques and Their Applications." p. 269 Wiley-Interscience (1971).

28. R. Gronsky. Ph.D. Thesis, Berkeley (1976).

29. D. R. Diercks, C. A. Wert. Met. Trans. 3, 1699 (1972).

30. D. R. Mosher, D. R. Diercks, C. A. Wert. Met. Trans. 3, 3077 (1972).

31. R. K. Viswanadham, C. A. Wert. Met. Trans. 5, 123 (1974).

32. R. K. Viswanadham, C. A. Wert. J. Less-Comm. Met. 48, 135 (1976).

33. J. W. Christian. "The Theory of Phase Transformations in Alloys" Pergamon Press (1965).

34. K. H. Westmacott, M. I. Perez. Submitted Nov. (1978) to J. Nucl. Mat.

35. E. K. Storms. "The Refractory Carbides." p. 91 AC. Press, New York (1967).

36. D. A. Vaughan, O. M. Stewart, C. M. Schwartz. Trans. Aine 221, 937 (1961).

37. L. E. Toth. "Transition Metal Carbides and Nitrides." p. 42, AC. Press, New York (1971).

38. V. K. Heikkinen, T. J. Hakkarainen. Phil. Mag. 8, 237 (1973).

39. A. Kelly, G. W. Groves. "Crystallography and Crystal Defects" Addison-Wesley (1970).

40. Pearce, W. Kriven, P. Rez. Program "Stereo". Unpublished. For similar programs, see: O. Johari, G. Thomas. The Stereographic Projection and Its Applications, Vol. IIA in Techniques of Metals Research. Ed. R. F. Bunshah, published by Interscience Publishers, New York, 1969.

41. D. I. Potter. J. Less-Comm. Met. 31, 299 (1973).

42. A. Deschanvres, A. Maisseu, G. Noufi, J. Vicens. J. Less-Comm. Met. 34, 237 (1974).

43. R. A. Swalin. ACTA Cryst. 10, 473 (1957).

44. P. G. Partridge. Met. Rev. 118, 1969 (1967).

45. R. Gevers, J. van Landuyt, S. Amelinckx. Phys. Stat. Sol. 11, 689 (1965).

46. A. G. Khachaturyan. "Order-Disorder Transformations in Alloys." p. 114, H. Warlimont, ed., Springer, Berlin (1974).

47. V. F. Petrunin, V. A. Somenkov, S. S. Shil'shtein, A. A. Chetkov. Sov. Phys.-Cryst. 15, 137 (1970).

48. T. Schober. Proc. Second Int. Congress on H in Metals, 1 (1977).

49. H. Asano, R. Yamada, M. Hirabayashi. Trans. JIM 18, 155 (1977).

50. T. Schober, A. Carl. Scr. Met. 11 397 (1977).

51. O. van der Biest, G. Thomas. ACTA Cryst. A 33, 618 (1977).

52. J. Völkl, G. Alefeld. Chap. 5 in Diffusion in Solids. Ac. Press (1975).

53. D. Hull, D. C. Wyne. Proc. 3rd European Regional Conference on Electron Microscopy (1964) 239.

54. L. Stals, J. van Landuyt. Phys. Stat. Sol. 5 (1964) K1.

55. J. van Landuyt, R. Gevers, S. Amelinckx. Phys. Stat. Sol. 13 (1966) 467.

56. K. Abe, H. Yoshinaga, S. Morozumi. Trans. JIM 17, 551 (1976).

57. G. Hörz, K. Lindenmaier, R. Klaiss. J. Less-Comm. Met. 35, 97 (1974).

58. Kopyleva in The Refractory Metal Carbides. Vol. 2, by E. K. Storms AC. Press, New York (1967).

59. E. Fromm. J. Less-Comm. Met. 14, 113 (1968).

60. H. Jehn, G. Hörz. Z. Metallk. 67, 417 (1976).

61. E. Fromm, G. Spaeth. Z. Metallk. 67, 410 (1976).

62. E. Fromm. Z. Metallk. 67, 413 (1976).

63. H. J. Grabke, G. Hörz. Ann. Rev. Mat. Sci. 7, 155 (1977).

64. L. E. van Torne, G. Thomas. ACTA Met. 12, 601 (1964).

65. G. Hörz, K. Lindenmaier, R. Klaiss. J. Less-Comm. Met. 35, 77 (1974).

66. K. H. Jack in "Heat Treatment '73" Proc. Conf. Joint Committee Iron and Steel Inst., Inst. Metals, Inst. Metall., ' ndon, Dec. (1973).

67. "Vacancies and Interstitials in Metals." A. Seeger, Ed., North Holland (1970).

68. M. Lomer. "Vacancies and Point Defects in Metals and Alloys." J. Inst. Met. Symp. 23, 79 (1957).

69. W. Glaeser, et. al. Phys. Stat. Sol. 35, 367 (1967).

70. C. Homan. "Diffusion in BCC Metals." Amer. Soc. Metals. 149, (1965).

71. A. Kelly, R. B. Nicholson. "Strengthening Methods in Crystals." Elsevier, New York (1971).

72. H. Y. Chang, R. K. Viswanadham, C. A. Wert. Met. Trans. 5, 1907 (1974).

73. H. Y. Chang, C. A. Wert. Met. Trans. 5, 1671 (1974).

74. S. C. Agarwal, A. Taylor, S. B. Gerber. "Radiation Effects and Tritium Technology for Fusion Reactors," Gatlinburg Conference-- 750989 I, 93 (1975).

75. L. M. Brown, G. R. Woolhouse. Phil. Mag. 17, 781 (1968).

76. M. F. Ashby, L. Johnson. Phil. Mag. 20, 1009 (1969).

77. B. J. Burke, D. Stuckey. Phil. Mag. 31, 1063 (1975).

78. R. Sinclair, G. Thomas. Met. Trans. 9A, 373 (1978).

79. T. Federighi, G. Thomas. Phil. Mag. 7, 127 (1962).

Table 2: Percent Mismatch for Approximately Parallel Planes Near the Burgers Orientation Relationship

System		Ta/Ta_2C	V/V_3N	Ta/Ta_2N	Nb/Nb_2N	Nb/Nb_2C	V/V_2C	W/W_2C	Mo/Mo_2C
$(uvw)_{bcc}$	$(hkil)_{hex.}$								
$1\bar{1}0$	$01\bar{1}0$	+15.1	+14.0	+13.1	+13.4	+16.0	+16.0	+15.7	+17.2
$1\bar{1}1$	$11\bar{2}0$	-18.6	-19.4	-20.0	-19.8	-18.0	-18.0	-18.2	-17.1
$00\bar{2}$	$\bar{2}110$	- 6.0	- 6.9	- 7.7	- 7.4	- 2.6	- 5.3	- 5.6	- 4.3
110	0002	+ 5.8	+ 5.7	+ 5.5	+ 7.0	+ 6.6*	+ 6.0*	+ 0.9*	+ 6.4
$10\bar{1}$	$\bar{1}101$	+ 1.2*	+ 0.4*	- 0.3*	+ 0.2*	+ 1.9	+ 1.8	+ 2.9	+ 2.7
$2 \times 1\bar{1}2$	$\bar{1}100$	- 0.3	- 1.2	- 2.1	- 1.8	+ 0.5	+ 0.5	+ 0.2	+ 1.5
	a_{hex}	3.106	2.835	3.050	3.055	3.126	2.884	2.990	3.012
	c_{hex}	4.945	4.551	4.928	4.994	4.972	4.565	4.720	4.736
	a_{bcc}	3.303	3.045	3.303	3.300	3.300	3.045	3.165	3.147
	SHAPE	RODS	PLATES	PLATES	PLATES				
	FAULTS	APB'S	TWINS	TWINS	TWINS	FAULTS			

* Planes are exactly parallel in the reported orientation relationship.

LIST OF FIGURES

Figure

Figure

9   Grain boundary in Ta-0.5 at-%C quenched and aged 17 hrs at
~500°C in UHV. Note large precipitate-free zone and absence
of grain boundary precipitates.

10   Typical microstructure of material shown in fig. 9. Note the
mottled background and the large coherency strain fields. Most
particles are attached to a lattice dislocation.

11   High magnification view of the same material as in f's. 9 and
10, showing change in background structure of coherent pre-
cipitates in different diffracting conditions.

       The selected area diffraction pattern shows weak extra spots
due to the ordered hexagonal structure (β-Ta$_2$C) of the coherent
precipitates.

12   (110) tilted beam lattice fringe image of coherent precipitate
and matrix in the quench-aged (17 hrs at ~500°C) material. No
variations in fringe spacing are measurable near the matrix
precipitate interface. The inset picture shows the precipitate
at lower magnification, magnified area encircled.

13   Ta-0.5 at % C, quenched at 2500°C per sec and aged 144 hrs
at ~800°C in UHV (p = 10^{-8} torr), showing large needle-shaped
precipitates and heavy dislocation substructure arranged in cell
walls.

14   Single precipitate in a thin part of the quench-aged material
of fig. 13. Note needle shape, Moiré fringes in the interface
and weak (0001) reflections due to carbon ordering.

15   Comparison of the different observed types of carbon ordering
in the interstitial sublattice of a hexagonal host lattice.
Only the interstitial sublattice is shown. L$_3'$ RANDOM is the high
temperature α-Ta$_2$C structure which orders into the C6 type of
β-Ta$_2$C at low temperature. After ref. 35.

16   String of dislocation loops punched out by the precipitate in
the bottom part of the picture. Ta ~ 1 at -%C, 2 hrs at 2000°C,
cooled at ~1°C sec^{-1} in a vacuum of p=10^{-6} torr.

17   Ta ~ 0.5 at -%C, 72 hrs at 1400°C, cooled at 1°C sec.$^{-1}$ in
a vacuum of p ≈ 10^{-6} torr. The dislocation loops near the
needle shaped particle at the bottom intersect the surface
(curved arrow). The straight arrow points to a string of
particles located inside of dislocation loops (out of contrast
here).

18   Contrast experiment on loop/particle configuration of fig. 17.
Loops are edge-on in c). Note curved fringes in the weak beam
image in e).

Figure

19   Stereographic projection of the orientation relationship between hexagonal Ta_2C (4 indices, dotted lines) and cubic matrix (indices in *italics*, solid lines). Note that only $(10\bar{1})$ and $(\bar{1}101)$ are exactly parallel. Stereogram plotted to scale for c/a = 1.592 of β-Ta_2C.[40]

20   Selected {111} diffraction patterns of precipitates and matrix simultaneously. The corresponding great circles are shown in the stereogram in d). The spots marked T in c) arise from twinning of the precipitate (see fig. 24).

21   Selected {110} composite diffraction patterns of precipitate and matrix. The corresponding great circles are outlined in the stereogram in d). Fig. c) coincides with the axis of the stereogram—see also fig. 19.

22     $(00\bar{1})$ composite diffraction pattern of precipitate and matrix. The corresponding great circle is outlined in the stereogram in b). An $(0\bar{1}0)$ projection is shown in fig. 25f.

23   Contrast experiment on three-particle configuration. The diffraction patterns show that the three particles are rotated 70 5° with respect to each other. Note Moiré fringes in 2) and 3) and interface dislocations.

24   Ta $\sim$ 0.5 at -%C, 72 hrs at 1400°C, cooled at $\sim$1°C sec^{-1} in p = 10^{-6} torr, showing $(\bar{1}101)$ $[1\bar{1}02]$ twinning. Twins are marked T. The dark field image in b) was taken with $g(\bar{1}01)$, common to the matrix and both twin related parts of the precipitate. The corresponding diffraction pattern is displayed in fig. 20c. Interface dislocations are arrowed.

25   Ta $\sim$ 1 at %C, 2 hrs at 2000°C cooled at $\sim$1°C sec^{-1} in p = 10^{-6} torr. Contrast experiment showing nature of interfacial dislocation network contained in the matrix.

26   Ta $\sim$ 1 at-%C, 2 hrs at 2000°C, cooled at $\sim$1°C sec^{-1} in p = 10^{-6} torr. The dark field shows conservative antiphase boundaries ending at dislocation with a c-component.

27   Material as in fig. 26; lattice image, tilted illumination showing precipitate matrix interface edge-on near an $(00\bar{1})$ orientation. The interface is exactly parallel to the close packed planes and fringe spacing correspond to equilibrium plane spacings in the two structures. Precipitate and matrix are marked p and m, respectively.

28   Material as in fig. 24; lattice images of precipitate-matrix interface edge-on near a $(1\bar{1}\bar{1})$ orientation. $(0002)|(110)$ fringes are continuous across the interface between matrix m and precipitate p in the left fig. Burgers circuits at A and B show closure failure. The right figure shows ledges following close packed matrix planes.

Figure

29   Material as in fig. 26. Contrast experiment revealing the
      nature of the straight dislocations in the short interface,
      arrowed. (001) surface orientation. Note conservative antiphase
      boundaries in c).

30   Material as in fig. 26. Lattice image of the defect structure
      in the short interface tilted illumination. Orientation near
      (1$\bar{1}$1). The inclined interface between the precipitate p and
      the matrix m shows optically dense areas every 19th (110)
      spacing (arrows), corresponding to the dislocations analysed
      in fig. 29.

31   Magnified view of lattice image in fig. 30. The inset dif-
      fraction pattern shows the orientation (see stereogram, fig 19.
      The full rotation of 1.5° between (0001) and (110) planes can
      be measured directly. The fringe spacing corresponds to the
      equilibrium lattice plane spacing.

32   δ-contrast at domain boundaries in pure tantalum foils con-
      taminated by hydrogen during chemical polishing. Note the
      boundary parallel to [0$\bar{1}$1], seen edge-on.

33   Selected area diffraction patterns of the three domains shown
      in fig. 32 showing extra spots at different 1/2 ⟨110⟩ positions
      for each domain.

34   Top: reciprocal lattice of tantalum hydride as derived from fig. 33.
      Bottom: corresponding real space lattice. Only the hydrogen
                positions in its interstitial sublattice are shown.

35   The six different possibilities of arranging an ordered hydrogen
      layer structure in the tetrahedral interstitial sublattices of
      the bcc host lattice. Periodic host atom displacements are
      shown by arrows in a). (001) projection. The large circles
      denote Ta host atoms (after ref. 47).

36   Three-dimensional representation of two (60°) orientations of
      the Ta$_2$H structure (fig. 35a), related by (1$\bar{1}$0) mirror symmetry.
      Outlined unit cell has monoclinic symmetry. The small ortho-
      rhombic distortion is not shown.

37   Top left: typical morphology of mobile domain boundaries in
      the hydride lattice of tantalum.
      Top right and bottom: contrast experiment showing coherent
      nature of domain boundary separating the domains on the left
      and the right. The relative orientation of the ordered lattice
      on both sides of the boundary is shown in fig. 36.

Figure

38   (001) projections of the two orientations of the hydride lattice
      shown in fig. 36. The projected unit cells are marked by heavy
      outlines. Only hydrogen atoms are shown. Their z-coordinate
      is given by the filled fraction of the circle. For example,◐
      denotes a hydrogen atom at one quarter of the total height of
      the ordered unit cell (fig. 36), i.e., at one half of the height
      of the disordered unit cell.

39   In situ cooling experiment on pure Ta-foil thinned chemically
      at 0°C. Top row of diffraction patterns: no hydride ordering
      is present at room temperature. Micrographs and center diffraction
      pattern: precipitation of hydride upon cooling to liquid
      nitrogen temperature. Bottom diffraction pattern: after
      dissolution of the hydride upon heating to room temperature.

40   Homogenizing treatments in ref. 2 (symbol o), ref. 6 (symbol λ)
      and ref. 5, (symbol +). Solubility limit after ref. 57.

41   Artifacts in thin foil preparation of Ta-0.5 at ~%C, heat
      treated as in ref. 5.
      (a) bright field picture showing electropolished foil with
           Ta_2C precipitate.
      (b) Dark field picture of chemically thinned foil with holes
           due to etching of precipitates. Note dislocation loops
           in both cases (arrowed).

42   Comparison of (001) and (1$\bar{1}$1) diffraction patterns of the
      literature on $Ta_{64}C$ and $Ta_{12}O$.

      (a) Ta – 1.53 at.~%C   "$Ta_{64}C$"   ref. 5
      (b) Ta – 1.82 at.~%C   "$Ta_{64}C$"   ref. 2
      (c) Ta – 3.3 at.~%O $Ta_{12}O$ ref. 17
      (d) Ta – 3.3 at.~%O $Ta_{12}O$ ref. 17
      (e) Ta   1 at.~%C   "$Ta_{64}C$"   ref. 6

      Note the weakness of the 1/2{440} and the absence of 1/2 {800}
      spots in all cases.

2.34 Å

b

g 200

0.1μ

001

110

2̄11

321̄

000

11̄0

231̄

115̄

WB g/4g

BF

$\bar{1}\bar{1}0$

0.1 μ

Fig. 7

Fig. 3

0.5μ

DF

0.1μ

g 011

Fig. 11

XBB 730-15223

Fig. 12

Fig. 15

L'_3 Random

$C\hat{6}$ Type
(β-Ta_2C)

$CaCl_2$ Type
(Co_2C)

ϵ-Fe_2N Type

ζ-Fe_2N Type

ξ-Nb_2C

⊗ Interstitial site occupied with probability $\frac{1}{2}$

● Interstitial site occupied

○ Interstitial site vacant

XBL 7812-6258

Fig. 16

XBB 789 12558

BF g $\bar{1}0\bar{1}$

a

b

c

d

e

XBL78 12-6259

Fig. 19

XBB 791-45

Fig. 20

XBB 791-46

Fig. 21

Fig. 22

XBB 791-47

Figure 1: g 011

Figure 2: g 110, a, b, c

Figure 3: g 101, 0.1μ

Insets: a, b, c

a (left panel): labels — $01\bar{1}$, $\bar{1}10$, $\bar{1}01$, T, T, $g\ \bar{1}10$, BF

b (right panel): labels — $g\ \bar{1}01$, DF

Fig. 25

XBB 730-15069

BF g 110

DF g0001

0.1μ

Fig. 26

XBB 760 12293

(00$\bar{1}$)

Fig. 37

Fig. 2

Fig. 29

(1̄1̄1̄)

0001

1.5°

110

Hydrogen Atoms
at z =

0, 1	⚪
1/4	◓
1/2	◑
3/4	⬤

XBL 7812-6277

Fig. 35

Fig. 36

XBL 782-7207

XBB 762-1386

Fig. 37

XBL 782-7206

Fig. 38

XBB 782-1387

Fig. 39

XBL 7812-13710

Fig. 40